PNNL-25066

Pacific Northwest
NATIONAL LABORATORY

*Proudly Operated by Battelle Since 1965*

# Hybrid Enrichment Verification Array: Module Characterization Studies Version 2

## December 2015

MA Zalavadia
LE Smith
BS McDonald
JA Kulisek
EK Mace
NS Deshmukh

U.S. DEPARTMENT OF ENERGY

Prepared for the U.S. Department of Energy
under Contract DE-AC05-76RL01830

PACIFIC NORTHWEST NATIONAL LABORATORY
*operated by*
BATTELLE
*for the*
UNITED STATES DEPARTMENT OF ENERGY
*under Contract DE-AC05-76RL01830*

**Printed in the United States of America**

**Available to DOE and DOE contractors from the**
**Office of Scientific and Technical Information,**
**P.O. Box 62, Oak Ridge, TN 37831-0062;**
**ph: (865) 576-8401**
**fax: (865) 576-5728**
**email: reports@adonis.osti.gov**

**Available to the public from the National Technical Information Service**
**5301 Shawnee Rd., Alexandria, VA 22312**
**ph: (800) 553-NTIS (6847)**
**email: orders@ntis.gov <http://www.ntis.gov/about/form.aspx>**
**Online ordering: http://www.ntis.gov**


This document was printed on recycled paper.
(8/2010)

PNNL-25066

# Hybrid Enrichment Verification Array: Module Characterization Studies Version 2

MA Zalavadia
LE Smith
BS McDonald
JA Kulisek
EK Mace
NS Deshmukh

December 2015

Prepared for
the U.S. Department of Energy
under Contract DE-AC05-76RL01830

Pacific Northwest National Laboratory
Richland, Washington 99352

# Summary

In recent years, the International Atomic Energy Agency (IAEA) has pursued innovative techniques and an integrated suite of safeguards measures to address the verification challenges posed by the front end of the nuclear fuel cycle. Among the unattended instruments currently being explored by the IAEA is an Unattended Cylinder Verification Station (UCVS) that could provide automated, independent verification of the declared relative enrichment, $^{235}U$ mass, total uranium mass and identification for all declared $UF_6$ cylinders in a facility (e.g., uranium enrichment plants and fuel fabrication plants). Under the auspices of the United States and European Commission Support Programs to the IAEA, a project has been undertaken to assess the technical and practical viability of the UCVS concept. At the core of the viability study is a long-term field trial of a prototype UCVS system at a fuel fabrication facility. A key outcome of the study is a quantitative performance evaluation of two candidate nondestructive assay (NDA) methods being considered for inclusion in a UCVS: Hybrid Enrichment Verification Array (HEVA) developed by Pacific Northwest National Laboratory, and Passive Neutron Enrichment Meter (PNEM) developed by Los Alamos National Laboratory.

The work presented in this report is focused on the characterization and refinement of the HEVA approach, which combines the traditional 186-keV $^{235}U$ signature with high-energy prompt gamma rays from neutron capture in the detector and surrounding collimator material, to determine the relative enrichment and $^{235}U$ mass of the cylinder. The design of the HEVA modules (hardware and software) deployed in the current field trial builds on over seven years of study and evolution by PNNL and consists of a ø3″×3″ NaI(Tl) scintillator coupled to an Osprey digital multi-channel analyzer tube base from Canberra. In comparison to previous versions, the new design boosts the high energy prompt gamma-ray signature, provides more flexible and effective collimation, and improves count rate management via commercially available pulse-processing electronics with a special modification prompted by PNNL.

The Canberra Osprey was selected for use in HEVA for its high degree of flexibility in parameters, robust power and communications options, compact form factor, and familiarity within the IAEA. This report describes the motivation and process for defining Osprey parameter settings suitable for the application of HEVA to the UCVS scenario, including: digital trapezoidal filtering, baseline restoration, fast discriminator, pile-up rejection, live-time correction and spectrum acquisition time. The effects of each of these parameters on acquired gamma-ray spectra were studied over a range of count rates that span the expected values for cylinder assay. Results presented here indicate that systematic uncertainties introduced by Osprey pulse-processing parameters will be insignificant in the overall HEVA uncertainty budget, so long as input count rates are maintained less than approximately 50 kcps and Osprey settings are carefully chosen. These findings have informed the hardware and software configurations utilized in the UCVS prototype and long-term field trial.

At the core of the HEVA methodology is the high energy prompt gamma-ray signature that serves as an indirect method for the measurement of total neutron emission from the cylinder. A method for measuring the intrinsic efficiency of this “non-traditional” neutron signature, and the results from a benchmark experiment are presented. Also discussed are potential perturbing effects on the non-traditional signature, including short-lived activation of materials in the HEVA module. Modeling and empirical results are presented to demonstrate that such effects are expected to be negligible for the envisioned UCVS implementation scenario.

# Acknowledgments

Funding for this work has been provided by the U.S. National Nuclear Security Administration's (NNSA) Office of Nonproliferation and Arms Control (NA-24) and the Next Generation Safeguards Initiative, and the U.S. Support Program (USSP) to the IAEA. The authors are appreciative to Karyn Durbin and Anthony Belian of the NNSA, and Joseph Carbonaro of Brookhaven National Laboratory and the USSP for their support and guidance of this project. The authors would also like to thank James Ely of the IAEA for his oversight of the UCVS development, and Peter Schwalbach and James Morrissey of Euratom safeguards for their advice and collaboration.

# Acronyms and Abbreviations

| | |
|---|---|
| PNNL | Pacific Northwest National Laboratory |
| HEVA | Hybrid Enrichment Verification Array |
| UCVS | Unattended Cylinder Verification Station |
| ROI | Region of Interest |
| MCNP | Monte Carlo N-Particle |
| ADC | Analog to Digital Conversion |
| MCA | Multi-Channel Analyzer |
| DTB | Digital Tube Base |
| NIM | Nuclear Instrument Module |
| BLR | Base-Line Restoration |
| FWHM | Full Width Half Maximum |
| LLD | Lower Level Discriminator |
| PHA | Pulse Height Analysis |
| PUR | Pile-Up Rejection |
| LTC | Live-Time Correction |
| FT | Flat-top Time |
| RT | Rise Time |
| CR | Count Rate |
| PGNAA | Prompt Gamma Neutron Activation Analysis |

# Contents

# Figures

# Tables

# 1.0 Introduction

The International Atomic Energy Agency's (IAEA's) current enrichment-plant safeguards approaches include attended weighing and nondestructive assay (NDA) of a subset of the plant's cylinder flow and inventory, collection of bulk uranium hexafluoride ($UF_6$) samples for destructive analysis, and environmental sampling for subsequent laboratory analysis. New safeguards measures that are more effective and cost-efficient than contemporary measures are needed, particularly for modern high-capacity plants [1]. Detection of prominent diversion scenarios could be improved at enrichment plants if the IAEA could monitor 100 percent of material flows and periodically calculate independent uranium and $^{235}U$ mass balances for the facility. However, limited human and financial resources preclude continuous inspector presence at the facility to measure all of the material flow, using today's attended methods. Further, the portable measurement methods currently used by inspectors have relatively low accuracy for the assay of relative $^{235}U$ enrichment, especially for natural and depleted $UF_6$, and no capability to assay the absolute mass of $^{235}U$ and total uranium in the cylinder, because of the highly localized nature of the instrument geometry and low-energy gamma-ray signature.

Unattended instruments capable of continuously monitoring material flows, and of performing the routine and repetitive measurements previously performed by inspectors without additional burden to operators, are central to the new safeguards approaches being considered by the IAEA [2] [3]. One of the instrumentation concepts being considered by the IAEA is an Unattended Cylinder Verification Station (UCVS) [3] [4]. According to the IAEA's current vision, UCVS units would be located at key intersections of cylinder movement between material balance areas, or at the operator's accountancy scales (in order to take advantage of the facility's cylinder weighing operations). The station would include technologies for cylinder identification, NDA of the cylinder contents, video surveillance and data transmission to an on-site computer and IAEA headquarters. A notional UCVS is illustrated in **Figure** 1

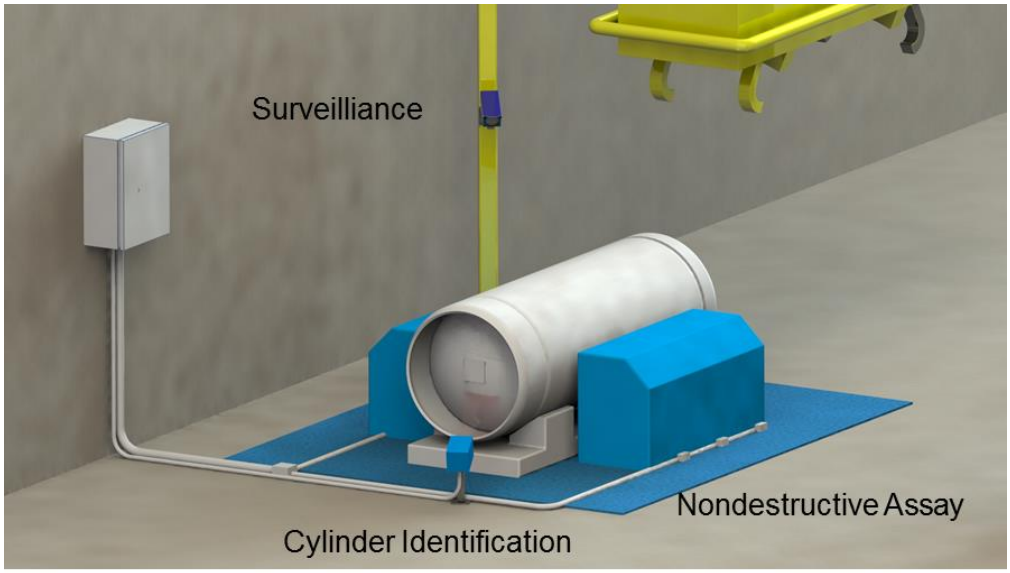


**Figure 1.** Conceptual design of an integrated UCVS that includes unattended NDA instrumentation (blue panels), camera surveillance and cylinder identification technology.

According to the IAEA, the NDA components of the UCVS will support several measurement objectives, including: unattended, independent assay of cylinder enrichment ($E_{cyl}$) and $^{235}$U mass ($M_{235}$) for product, feed, and tail cylinders; independent assay of total uranium mass ($M_U$) as a confidence-building measure on the authenticity of data from operator weighing systems; and the unattended application, verification, and re-verification of an "NDA Fingerprint" to maintain the verification pedigree of the cylinder contents and to verify that no partial removal of material has occurred during the cylinder's life at the facility [4, 5]. If the potential of the UCVS concept can be realized, such an instrument could significantly enhance the IAEA's efficiency in implementing safeguards approaches at large-capacity enrichment plants, while simultaneously improving effectiveness for deterring and detecting diversion of material from declared flow. A UCVS could also provide benefits to the operators, by easing and expediting the release process for product cylinders, and automating cylinder tracking [3].

Though the potential of a UCVS system is understood, its field performance and operational viability in commercial nuclear facilities where cylinders are handled has yet to be fully tested. Under the auspices of the United States and European Commission Support Programs to the IAEA, a project has been undertaken to assess the technical and practical viability of the UCVS concept. A key outcome of the study is a quantitative performance evaluation of two candidate nondestructive assay (NDA) methods being considered for inclusion in a UCVS: Hybrid Enrichment Verification Array (HEVA) developed by Pacific Northwest National Laboratory, and Passive Neutron Enrichment Meter (PNEM) developed by Los Alamos National Laboratory.

The work presented in this report is focused on the characterization and refinement of PNNL's HEVA method, one of the two candidate NDA approaches being studied in the UCVS project. This study builds on several years of HEVA development and field testing by PNNL, particularly the findings from a joint US-Euratom project in which prior versions of HEVA and PNEM were deployed in an enrichment plant for side-by-side testing. Among the findings from that 2013 study was that the earlier HEVA hardware and software required revision and further development in order to be considered suitable for unattended operation in a fuel cycle facility. For example, the collimator/neutron converter design had an unnecessarily high ratio of mass to sensitivity for the indirect neutron signature. Further, greater flexibility was needed in the collimator mechanical design to better manage the detector field of view so that count rates in each spectrometer can be maintained well below the region where pulse pileup and dead time begin to degrade the quality of the recorded spectra. The pulse-processing electronics used in prior HEVA prototypes were chosen because they were readily available at no cost to the project, not because they were optimal for this application. Commercially available digital photomultiplier tube bases, used routinely in similar medium-resolution gamma-spectroscopy applications throughout the NDA community, should be utilized. These findings motivated a redesign of the HEVA hardware and software, in preparation for UCVS field trials.

This report describes and assesses the revised HEVA modules. An overview of the HEVA method and latest module design is provided in Section 2. Section 3 discusses the process and outcome of selecting appropriate parameters for the pulse processing electronics. Section 4 consists of the details pertaining to the indirect neutron detection efficiency evaluation and benchmark experiment. Section 5 discusses the effects of neutron activation in the detection medium and its effect on the veracity of the non-traditional neutron signature utilized in HEVA. Conclusions and thoughts on potential future work are offered at the end of the report.

# 2.0 Overview of the HEVA method

The HEVA methodology is founded on the simultaneous detection of multiple radiation signatures. These signatures include the direct 186-keV emission from $^{235}U$ and the neutron-induced high-energy gamma rays. The latter, referred to as the 'non-traditional' signature, represents the total neutron yield. The non-traditional neutron signature can be calibrated to total $^{235}U$ mass ($M_{235}$) under the assumption that the behavior of the $^{234}U/^{235}U$ ratio is known for the $UF_6$ material being produced by the facility [6] [7] [8].

The direct 186-keV emission from $^{235}U$ is the "traditional" signature currently used by the IAEA in routine verification measurements via the use of handheld spectrometers. While the HEVA method collects the same traditional 186-keV signature as currently practiced by Euratom and IAEA, there are distinct differences in how the systematic variations, such as the variability in the cylinder wall thickness, are addressed. Via the use of multiple spectrometers, the collection area is much larger and distributed along the length of the cylinder in the unattended HEVA assay. The original hypothesis in early HEVA development was that this large-area, distributed measurement would 'average out' any significant wall-thickness effects on the traditional 186-keV signature. This hypothesis has been supported in several field campaigns [6] [9] [10].

As discussed earlier, the non-traditional signature refers to the high-energy prompt gamma-rays, which are produced from neutron interactions within the collimator and the detector. The primary source of neutrons emitted from $UF_6$ is the reaction $^{19}F(\alpha,n)$, where the dominant source of alpha particle is the decay of $^{234}U$. Prior investigations have shown that the prominent source of nontraditional neutron signal is from neutron capture in the iodine of the NaI spectrometer crystal and $^{56}Fe$ in the steel of the specially designed collimators. Sandwiching of polyethylene between layers of steel has proven to provide high neutron-gamma conversion efficiency while minimizing the mass of the HEVA collimator/converter design. The nontraditional neutron signal, $HEVA_{NT}$, is defined as the sum of counts in 3-8.5 MeV region of interest (ROI), and summed across all NaI(Tl) spectrometers. Further details are presented in [10].

The HEVA prototype utilized in the UCVS project consists of an array of three ø3″×3″ NaI(TI) spectrometers surrounded by specialized collimators consisting of concentric layers of steel and polyethylene. The front side of the collimator assembly is covered with a lead face plate (~ 1.35-cm thick) with a 2.54-cm wide opening (aperture) to allow a direct path to the detector for the 186-keV gamma-rays from $^{235}U$. The innermost layer around the detectors is a 0.64-cm thick lead layer designed to help manage the count rate and reduce contributions from high-energy gamma rays. The photomultiplier tubes (PMTs) on each of the three NaI(Tl) detectors are coupled to a Canberra Osprey digital tube base that includes several functions: PMT power, preamplifier, shaping amplifier, analog-to-digital conversion and a multi-channel analyzer. Figure 2 provides a cross-sectional depiction of the HEVA detector-collimator assembly.

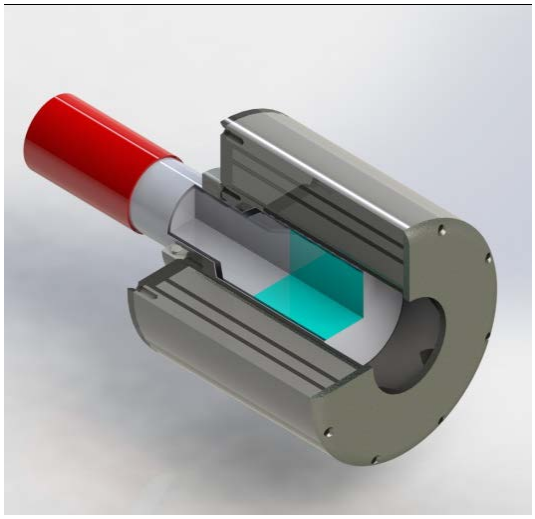

**Figure 2.** Cross-sectional rendering of the HEVA detector-collimator assembly. The Osprey digital tube base is depicted in red on the left, the NaI(Tl) crystal is the light blue object. Surrounding the crystal are layers of lead, polyethylene, and steel to manage the total count rate and enhance neutron-to-gamma conversion.

# 3.0 Estimation of Expected Count Rate

Characterization and refinement of the Osprey parameters must be done over a representative range of input count rates. For the cylinder assay scenario, the HEVA input count rate can vary significantly between cylinders, not just because of varying enrichment levels but also of the amount of non-$UF_6$ compounds and $^{238}U$ progeny on the bottom and walls of the cylinder. This material is often labeled "heels" and/or "wall deposits" (hereafter, "heels" for simplicity) and generally speaking, its volume and mass grow with the number of fillings that a given cylinder has experienced. Per cylinder certification regulations, cylinders must be cleaned of such material once its mass exceeds 11.3-kg [11].

Prior measurements of particularly "dirty" cylinders, using a different HEVA collimator design produced very high count rates and degrading effects (see Figure 3) associated with high dead times in the pulse processing electronics [9] [12]. To support the redesign of the HEVA module so that such issues could be avoided in the UCVS field trial, it was necessary that PNNL develop a capability to predict the effect of heels and wall deposits on HEVA count rate. To this end, a modeling effort was conducted to determine the range of count rates, per detector, that the Osprey would need to process.

The modeling effort was conducted using MCNP6, a Monte Carlo radiation transport code [13]. An assay of a Type 30B cylinder with 5 wt% $^{235}U$ enrichment and 11.3-kg heel was simulated. Per regulations, this is the maximum allowable mass for a heel in a Type 30B cylinder. The literature on heels composition was surveyed and considerable variability was found. Some sources noted that the heel consists of non-volatile impurities such as $UF_4$ and$UO_2F_2$ and that $^{238}U$ daughter products such as $^{234}Th$ remain in fluoride compounds after the heating and evacuation processes [14-16]. Other sources indicate that the majority of the heel is $UF_6$ [personal communications with industry managers]. The exact elemental composition is most likely of negligible consequence for the modeling study since the U isotopes within the heel are expected to contribute little to the overall detector response, compared to the U daughters from the previous fill. In addition, $UF_4$ and $UF_6$ are similar gamma-ray transport media.

In the count rate modeling for HEVA, the heel was considered to be $UF_4$ with a density of 6.7 $g/cm^3$, with all the uranium (U) daughter products from the previous $UF_6$ fill distributed uniformly throughout this heel [14]. The heel was defined (figure 3) as a uniform thickness of approximately 0.8 mm along the bottom of the inner cylinder wall and rising up to the fill level (determined by the cylinder weight limit and nominal $UF_6$ density). The modeling assumptions are considered conservative since a significant amount of the non-$UF_6$ material and all of its highly emitting daughters are presented in the field of view of each HEVA module, rather than pooled in the bottom of the cylinder where they would contribute little to the HEVA response. In addition, heels are typically less than 2-kg in practice [personal communication][17] but modeled here at a mass over five times higher. The worst-case scenario was also adopted for the decay of the daughters in the heel—it was assumed that the cylinder is assayed at a time when all of the U daughters are at their maximum activity. In practice, this is unlikely to be the case since the heels/wall deposit in a cylinder are an aggregation of the material from several cylinder withdrawal and filling sequences, and the effective decay constant of the heels is dominated by the decay rate of $^{234}Th$ (half-life of 24.1 days).

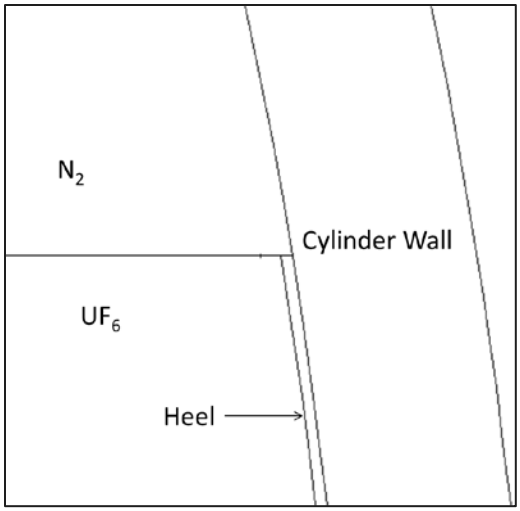


**Figure 3.** MCNP6 model of $UF_6$ cylinder with heel plated along inside wall.

The HEVA module and cylinder geometry were modeled in the same basic configuration used for the Westinghouse field trial. Namely, the Pb faceplate had a 2.54-cm diameter aperture and the front of the faceplate was located 2.5-cm from the wall of the cylinder. To characterize the adaptability afforded by the variable recess distance for the NaI spectrometer, recess values on the extremes were simulated: full recess (detector face 6-cm from back of faceplate) and no recess (0-cm from faceplate). In all cases, a lower level discriminator (LLD) of 50-keV was assumed in the pulse-processing electronics.

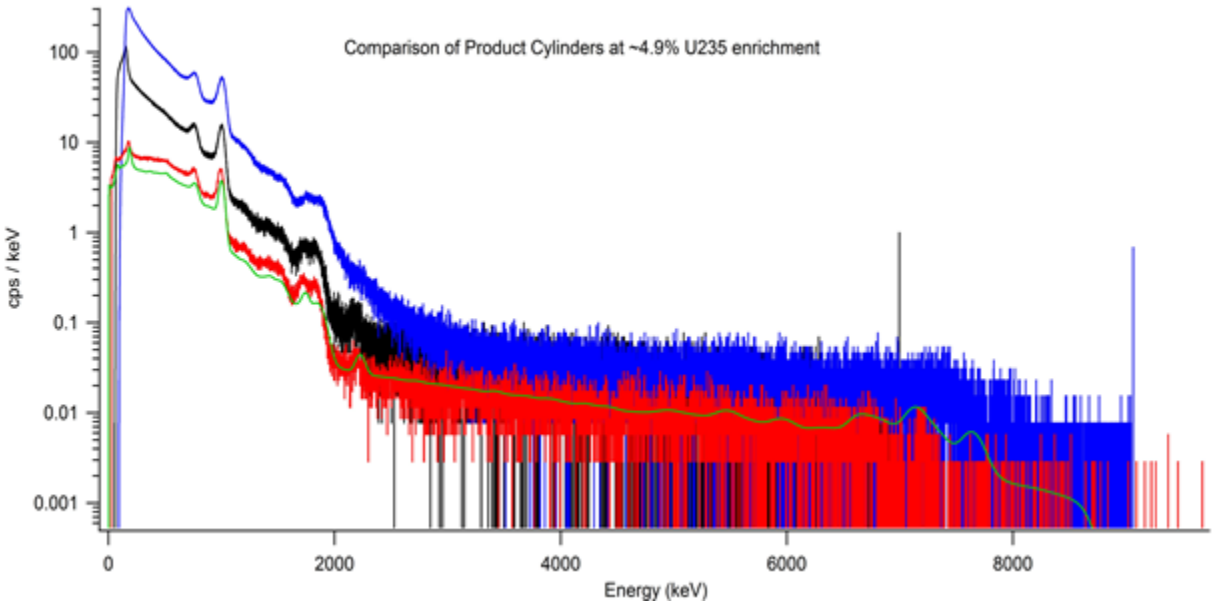


**Figure 4.** Example spectra for 5 wt. % Type 30B cylinders: Previous field campaigns using a prior HEVA module design measured cylinders with high wall deposits (blue) and lower wall deposits (black); MCNP simulations of the new module design for a cylinder with no wall deposits (green) and measured response for the new module design for a cylinder with unknown (but apparently relatively low) wall deposits (red).

Shown in Figure 5 are example results from that count rate modeling and analysis for cylinders with and without heels. As discussed previously, it is asserted that the with-heels simulations have worst-case assumptions in terms of the distribution of heel material in the detector's field of view, and the decay time of the daughters. As expected, the degree of detector recess has a significant effect on count rate: small recess distances produce larger count rates, while the maximum recess distance of 6-cm realizes significantly lower count rates, for the sample cylinder assumptions. But the greatest impact on count rate is the presence or absence of heels/wall deposits. Under the worst-case assumptions employed here, a "dirty" cylinder may have count rates nearly 20 times higher (over 150 kcps) than a clean cylinder with no significant heels/wall deposit.

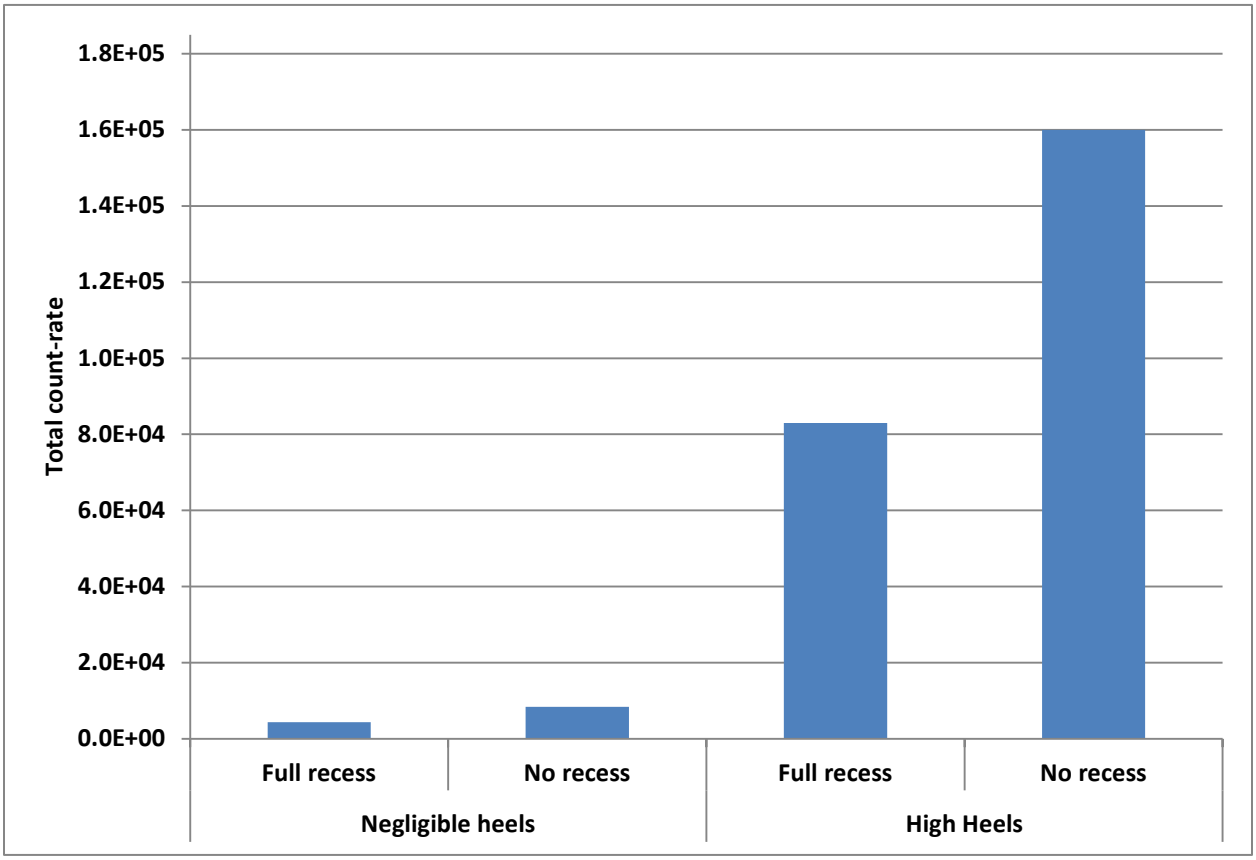


**Figure 5.** MCNP-based count rate predictions (cps) for a single HEVA module under different detector-recess and heels assumptions (negligible and a high, worst-case scenario).

For NaI spectrometers and commercially available digital pulse processing electronics, previous experience at PNNL and Canberra's published information on the Osprey indicate that count rates over approximately 50 kcps can be problematic in terms of accurate dead-time correction, pulse-pileup rejection, etc. One of the key objectives for this work is to provide empirical support for the definition of tolerable Osprey count rates for the HEVA modules, in terms of the systematic uncertainties introduced by various pulse-processing parameters. The modeling described above and the findings in this report, support PNNL's prescription for the HEVA collimation configuration in the UCVS trials.

# 4.0 Osprey Parameter Study

There are a number of parameters that affect the performance of the Osprey spectroscopic system, many of which offer an "automatic" mode. The primary objective of the Osprey parameter study was to understand the effects of each setting on the final observable, i.e. the gamma-ray spectra measured during each cylinder occupancy. As part of the HEVA characterization study, the following Osprey parameters were studied:

- **Trapezoidal filter parameters; Rise-time (RT) and Flat-top time (FT):** These digital pulse-shaping parameters have a large impact on the overall performance of the detection system with respect to energy resolution, dead time, and pulse pileup. Therefore, it is important to strike an appropriate balance between these effects for the range of expected count rates.

- **Baseline restoration (BLR):** A baseline shift can occur when the tail of one pulse does not return fully to the true zero level before the next is received. This phenomenon can lead to distortion of the pulse amplitude, which in turn can lead to degradation of the photopeak resolution. This effect is exacerbated at high count rates and thus, effective BLR methods are required to compensate in order to maintain the desired energy resolution performance.

- **Fast discriminator threshold:** The "fast" timing channel used to support pile-up rejection methods (see below) operates in parallel with the slower spectroscopic channel used to produce counts in the recorded spectrum. Any two events above the fast-discriminator threshold detected within a certain time window are considered as pile-up events and are removed from the pulse processing chain, thus eliminating the distorted pulses from the spectroscopic channel.

- **Pile-up Rejection Guard inspection interval (PUR Guard):** The PUR Guard parameter is the length of the time window used to determine pile-up events. This parameter interplays with the fast discriminator threshold to define the pile-up rejection capability for the Osprey.

- **Live-time correction (LTC):** Tests were defined to verify the accuracy of LTC over a range of count rates, since high-fidelity live-time correction is essential to reducing systematic uncertainties in the HEVA analysis methods.

- **Pulse Height Analysis (PHA) acquisition time:** The time interval used for acquiring spectra can have an impact on the fidelity of the dead-time-adjusted absolute count rate. While data analysis may encourage shorter acquisition times (e.g., 10 seconds), buffering and live-time-correction challenges often argue for longer acquisition time values.

While this is a large number of settings to explore, once they are defined they generally do not need to be modified and will not require any operator input during the field trial. Of note, the IAEA already has experience with the Osprey systems in multiple field trials for the unattended on-line enrichment monitor (OLEM) system [18], and Canberra is a stable supplier of instrumentation to the IAEA.

## 4.1 Trapezoidal Filter Parameters: Rise-time and Flat-top time

The Osprey employs a digital trapezoidal filter that allows the user to independently set the rise time (RT) and flat-top time (FT) according to the scintillator type and desired performance. Figure 6 depicts these timing parameters.

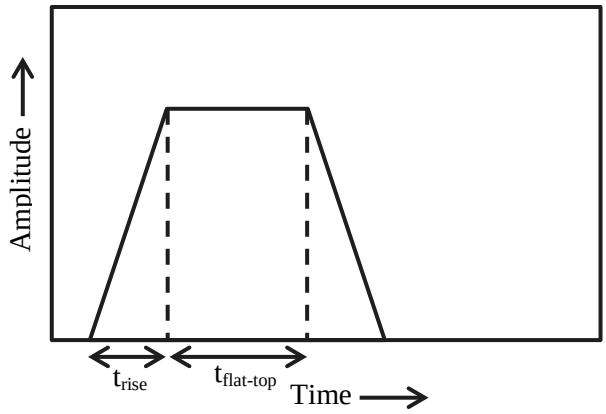


**Figure 6**. Digital pulse processing using a trapezoidal filter.

In theory, the RT of the trapezoidal filter should be long enough to allow collection of all scintillation light produced by the NaI(Tl) and therefore, maximize the signal to noise ratio. Since the decay constant of NaI(Tl) is 0.23μs, RT values of 1 μs or more are generally recommended from the signal-to-noise perspective, but that must be balanced by practical throughput considerations since longer rise/fall times lead to more dead time [19].

The FT accounts for the degree of variability in the charge collection time of the detector. Partial and variable collection of the charge produced by the detector can significantly degrade energy resolution in some detector types. In general, FT values that are too short can lead to ballistic deficit effects on energy resolution, particularly for large semiconductor detectors. In the case of inorganic scintillators such as NaI, each pulse is of the same length in time, without any dependence on the energy of the photon. Therefore, a single, relatively short FT value can be used.

Another potential impact of shortening the RT or FT (or both) is the degradation in peak resolution at lower operating temperatures. The scintillation light decay time increases significantly at temperatures below zero Celsius. Adequate pulse shaping time must therefore be allowed for full integration of the light yield in order to minimize the temperature related variations [20]. This is important for systems operating under wide temperature ranges but because low-temperature operation is not anticipated for the UCVS, variation in light output as a function of temperature was not considered nor tested.

In an Osprey, the total pulse shaping time, including the minimum spacing between pulses, required by the digital signal processor is 2.2 × RT + 2×FT [correspondence with Canberra]. There is an obvious tradeoff between improved energy resolution and minimized dead time. Longer pulse duration can increase the system dead time, which results in increased pulse pile up, degraded count rate performance

and poorer resolution due to the broadening of the photo-peak (associated with the pile-up). For NaI(Tl), the Canberra-recommended value for both RT and FT is approximately 1 μs [21].

Using these Canberra recommendations as a starting point, PNNL performed a series of tests to provide empirical support for the RT and FT values to be used in the HEVA modules during the UCVS field trial. The measurements were performed using five different Ospreys, each coupled to a ø3″×3″ NaI(Tl) detector. Note that only three HEVA modules will be used in the UCVS field prototype but a total of five detector systems were tested, out of which the best three were to be selected for the final design (the remaining two reserved as spares). Five-minute real-time and a $^{137}$Cs button source were employed. The following timing parameters were studied: RT= [0.6, 0.8, 1.0, 1.2, 1.4, and 1.6] μs and FT = [0.3, 0.4, 0.5, 0.6, 0.7, 0.8, 0.9, 1.0, 1.1, and 1.2] μs. These and other parameter studies were conducted with custom software that iteratively adjusts parameters and acquires data for fixed amounts of times. These measurements were conducted at low count rates (~ 2800 to 3100 cps) to reduce any effects of pileup, dead time, and baseline restoration, and maintain a focus on the FT and RT behavior. Table 1 lists all of the Osprey settings pertaining to these measurements.

**Table 1.** List of settings for RT/FT assessment.

| Parameter | Setting |
|---|---|
| HV (volts) | 640 to 700 |
| Total observed count rate (cps) | ~2900 - 3100 |
| Gain (Fine x Coarse) | 1.0 x 1.0 |
| Flat-top time (μs) | Variable |
| Rise-time (μs) | Variable |
| PUR Guard Time interval | 2.2x |
| LTC | On |
| BLR mode | Auto |
| Fdisc setting | Auto |
| Fdisc shaping | Normal |

Figure 7-11 show the relative full-width at half-maximum (FWHM) resolution at 662 keV for all five detectors, for various RT and FT values. The error bars on the full-width at half-maximum (FWHM) resolution span ±0.1 % of the measured value (one sigma, statistical only) and are not shown for ease of readability. Detector 1 exhibited the largest variability, and detector 3 had the worst energy resolution (~9% vs ~7% FWHM). While no investigation has been conducted into the likely cause of the resolution degradation, it is possible that reduced optical coupling between the crystal and the PMT, or to some degree of mechanical damage in the crystals themselves, has occurred. Based on this testing, detectors 1 and 3 were set aside as backups.

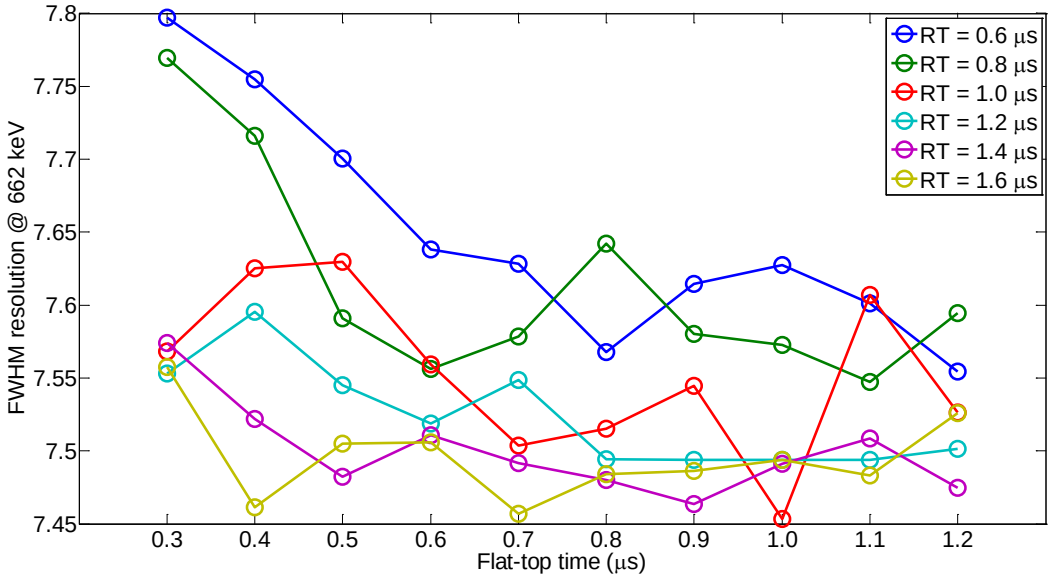


**Figure 7.** FWHM resolution at 662-keV at various RT and FT – detector 1.

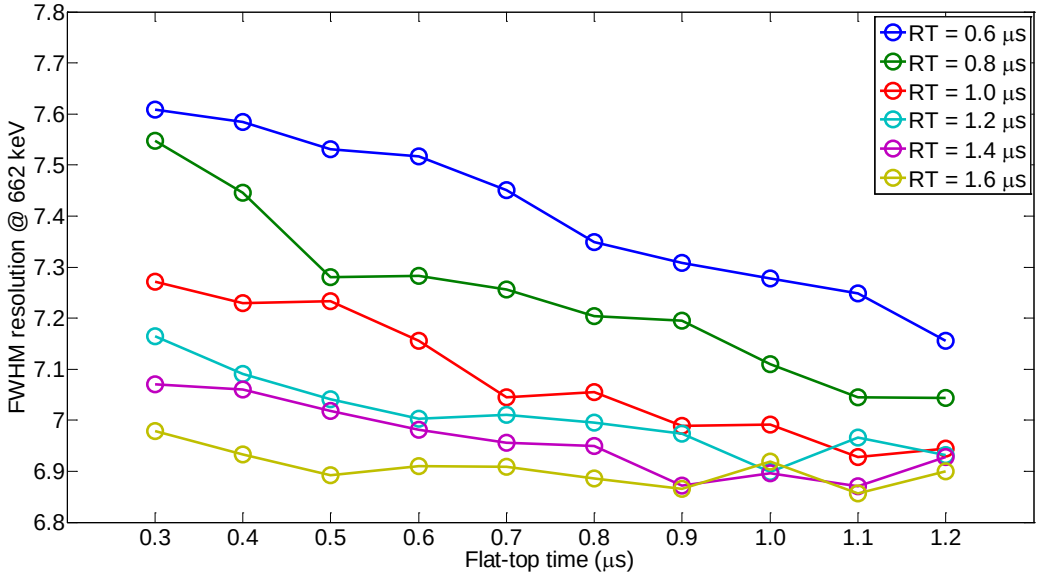


**Figure 8.** FWHM resolution at 662-keV at various RT and FT – detector 2.

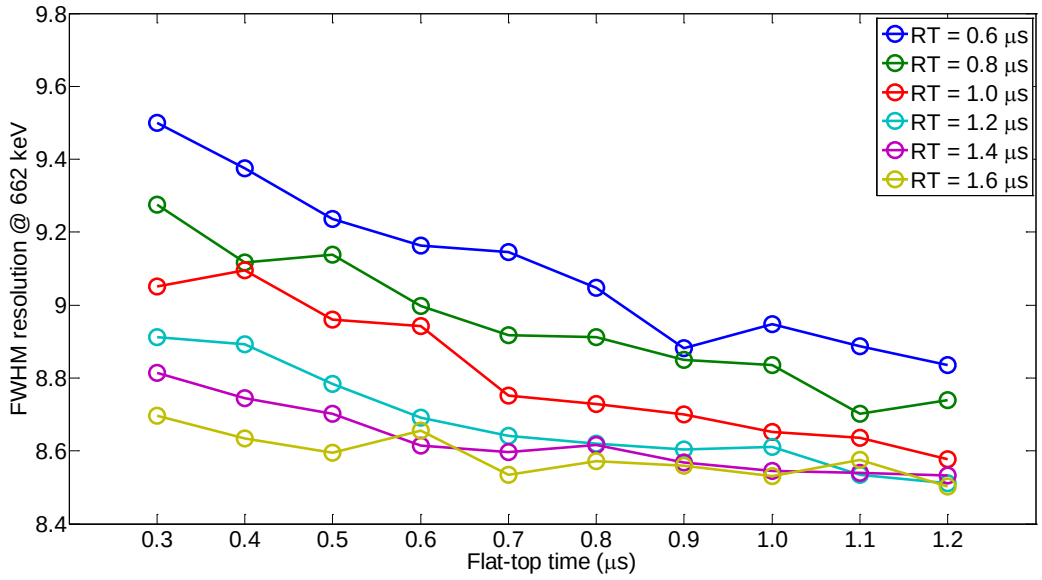


**Figure 9.** FWHM resolution at 662-keV at various RT and FT – detector 3.

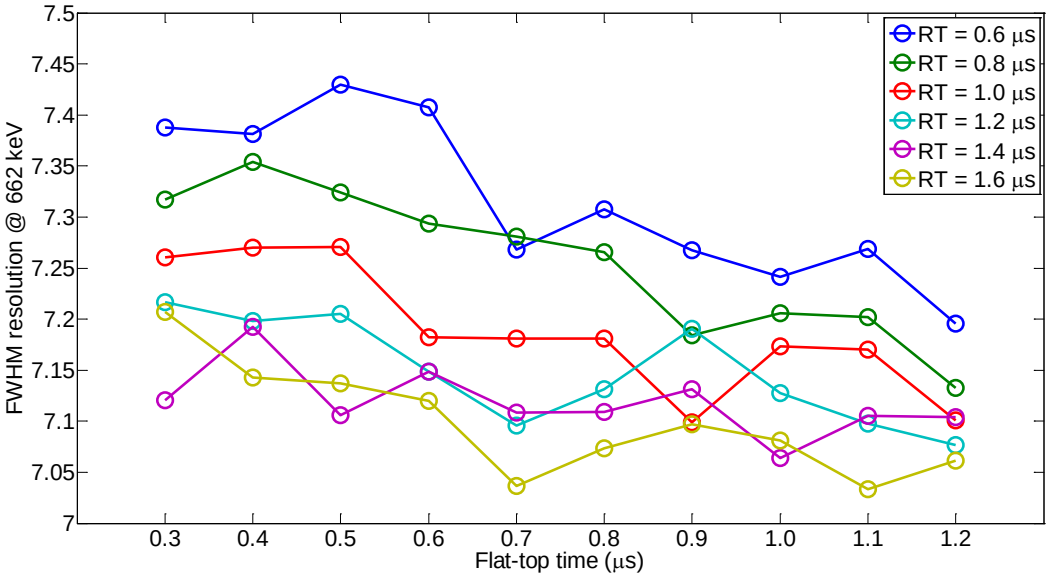


**Figure 10.** FWHM resolution at 662-keV at various RT and FT – detector 4.

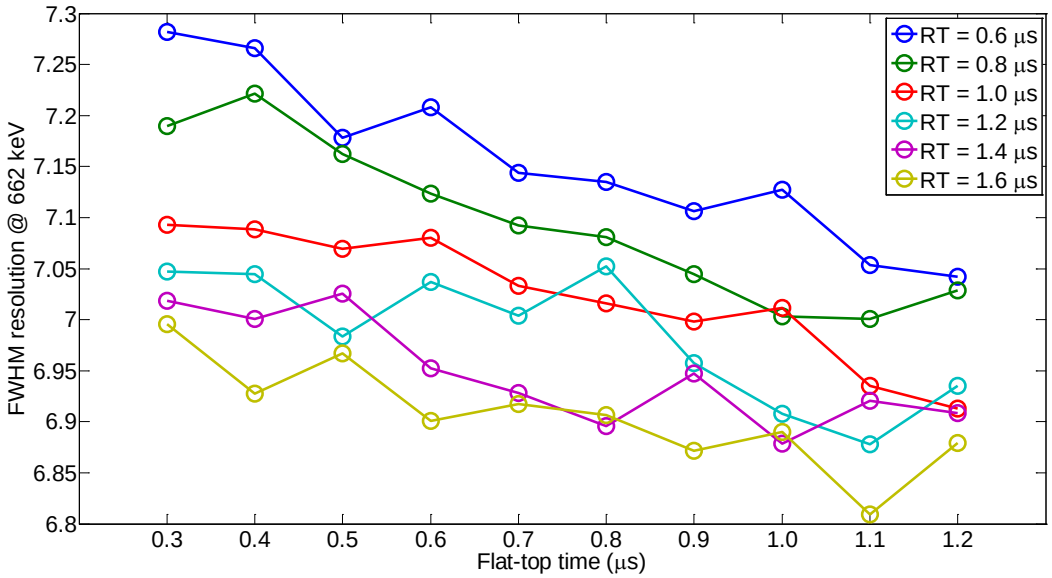


**Figure 11:** FWHM resolution at 662-keV at various RT and FT – detector 5.

As discussed above, theory predicts that the best energy resolution can be achieved by setting the shaping times longer to allow for full charge collection. Figures 7-11 support this hypothesis and show that for any given FT, the resolution can improve significantly as the RT increases. The resolution also improves with increasing FT (fixed RT), but with a weaker relationship. For example, Figures 7 - 11 indicate no significant loss in resolution when the FT is decreased from 1.0 to 0.5 µs, a trend confirmed in Table 2. These data suggest that reducing the FT to 0.5 µs, as compared to the Canberra recommendation of 1.0 µs, will have no appreciable effect on energy resolution, but will provide benefits in terms of detector throughput and live-time correction (see Section 4.6).

**Table 2.** Change in FWHM resolution (%) with increase in FT from 0.5 to 1.0 µs, assuming a rise time of 1.0 µs.

| Detector | FT = 0.5 µs | FT = 1.0 µs | Absolute Difference | Relative Difference (%) |
|---|---|---|---|---|
| **1** | 7.63 | 7.45 | 0.18 | 2.32 % |
| **2** | 7.23 | 6.99 | 0.24 | 3.35 % |
| **3** | 8.96 | 8.65 | 0.31 | 3.45 % |
| **4** | 7.27 | 7.17 | 0.10 | 1.35 % |
| **5** | 7.07 | 7.01 | 0.06 | 0.82 % |

Based on the analysis and interpretation above, FT and RT values of 0.5 and 1.0 µs, respectively, were selected for the UCVS prototype deployment.

## 4.2 Baseline restoration

Much of the relevant information in nuclear pulse processing is carried by the pulse amplitude, so it is important to measure this amplitude with the highest possible accuracy. Measurements of the pulse amplitude are made with respect to the true zero (system ground) by the analog to digital converter. Ideally, after a pulse has reached its maximum amplitude (i.e. the peak), its tail should return completely to a baseline at true zero. However, in practice and particularly at higher count rates, the baseline tends to shift above or below true zero. A series of pulses in quick succession (i.e., at high input rate) can lead to distorted pulse amplitudes because of baseline shift [20] [22]. For gamma spectroscopy applications, this means that ineffective baseline restoration (BLR) can lead to peak instability and shifts in peak centroid location at high counting rates. Effective BLR methods are therefore important to quantitative assay challenges, such as HEVA applied to cylinder assay.

In digital pulse processing, baseline restoration is often performed by subtracting the appropriate value of the baseline from the measured pulse amplitude. That baseline value is digitally sampled between pulses and multiple measurements are preferred for accurate compensation [20]. The Osprey is capable of performing the baseline restoration in four modes: *auto, hard, medium* and *soft.* Because the exact description of the mechanism associated with each of the options was not available from the manufacturer, an empirical method of change-and-effect was adopted to evaluate the functionality of the Osprey BLR feature and its allowable settings.

To assess the Osprey's BLR effectiveness, spectra were collected at each of the four settings with varying input count rates. The peak stability, i.e., peak centroid location, was then analyzed. Figure 12 and Figure **13** depict the results from tests in which four $^{137}$Cs spectra were collected at various input count rates ( by altering the source-detector stand-off distance), for each BLR mode. These tests were performed with a minimum and maximum PUR interval enabled in the Osprey (see Section 4.5). The peak stability should improve with high PUR guard interval since a larger fraction of the raw signal will be rejected, minimizing the effects of pileup on the peak width and centroid. Table 3 and Table 4 provide the parameter settings for this study.

**Table 3.** List of settings for BLR assessment (minimum pile-up rejection).

| Parameter | Setting |
|---|---|
| HV (volts) | 650 |
| Total observed count rate (cps) | ~35000 - 180000 |
| Gain (Fine x Coarse) | 1.0 × 1.0 |
| Flat-top time (μs) | 0.5 |
| Rise-time (μs) | 1.0 |
| PUR Guard Time interval | 1.1x (minimum) |
| LTC | Off |
| BLR mode | Variable |
| Fdisc setting | Auto |
| Fdisc shaping | Normal |

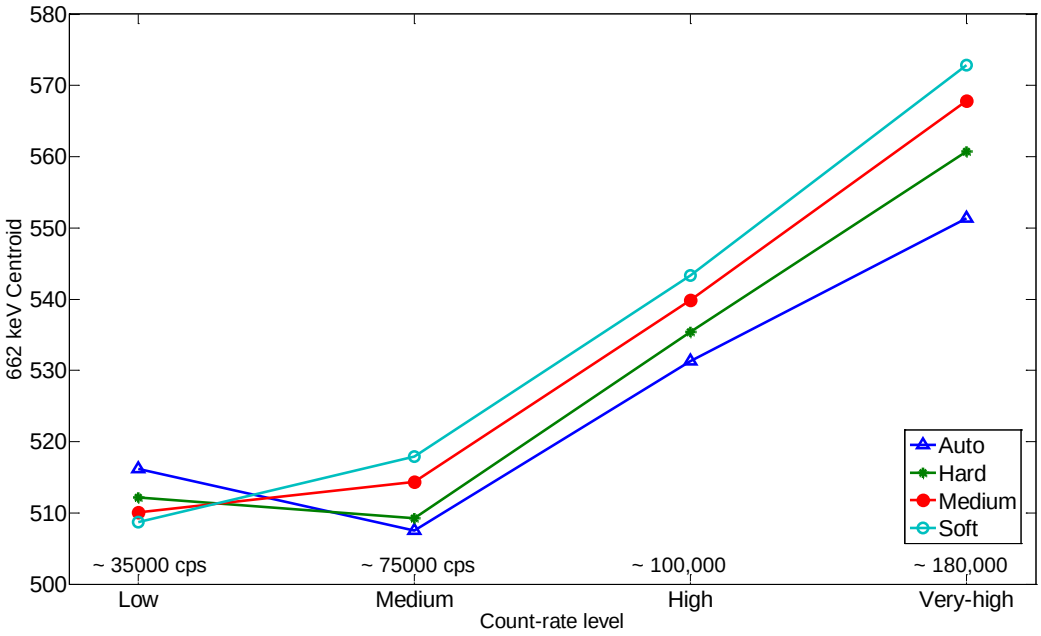


**Figure 12.** Centroid channel versus count rate (cps) at various BLR settings (with the pile-up guard set to the minimum, 1.1x).

**Table 4.** List of settings for BLR assessment (maximum pile-up rejection).

| Parameter | Setting |
|---|---|
| HV (volts) | 664.5 |
| Total observed count rate (cps) | ~20000 - 95000 |
| Gain (Fine × Coarse) | 1.0 x 1.0 |
| Flat-top time (µs) | 0.5 |
| Rise-time (µs) | 1.0 |
| PUR Guard Time interval | 2.5x (maximum) |
| LTC | on |
| BLR mode | Variable |
| Fdisc setting | Auto |
| Fdisc shaping | Normal |

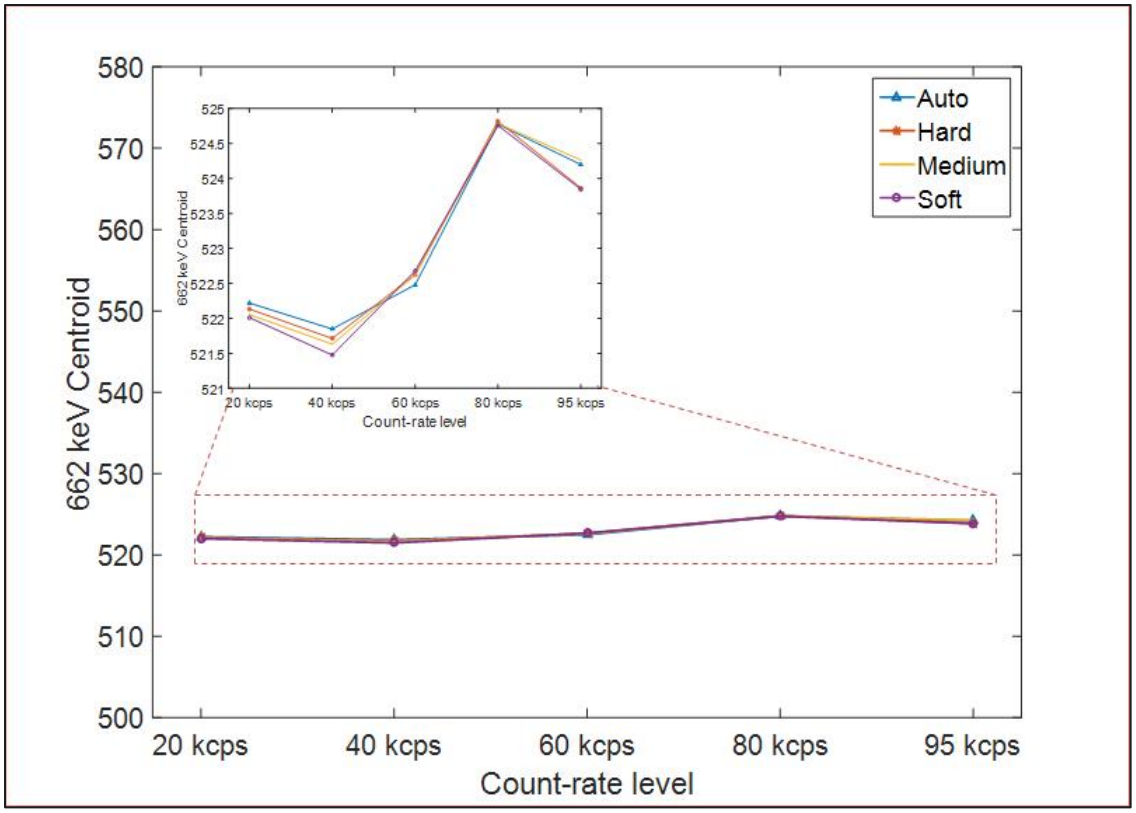


**Figure 13.** Centroid channel versus. Count rate (cps) at various BLR settings (with the pile-up guard set to the maximum, 2.5x).

Figure 12, where a minimum PUR interval is utilized, illustrates that there is significant variability in the peak centroid location as a function of count rate (~60 channels) and that centroid location is generally increasing with count rate. This indicates that low-amplitude pulses are piling up on the photopeak events, due to the short PUR interval. It appears that lower overall variability is achieved using auto mode. The next-best BLR setting in Figure 12, if full manual control is desired, is *hard*.

Figure 13, where a maximum PUR interval is utilized, shows that the different BLR settings change the peak centroid by less than a few channels up to 95 kcps. Note that the count rate range for the Figure 13 inset is different than for Figure 12. It is hypothesized that the long PUR interval is eliminating many of the low-amplitude pulses that create pileup in the full energy peak, resulting in better peak stability.

The results above do not clearly support one BLR setting over the other but one of the disadvantages of leaving this parameter in *auto* mode is that the BLR setting will continuously vary to get the best possible stability. While this feature may be desirable in some applications, it was decided that it may introduce unnecessary variability for the UCVS application. Therefore, a manual setting of *hard* was selected for the UCVS field trial. This study also indicates the benefit of using a long PUR interval, which is discussed further in a later section.

## 4.3 Fast Discriminator Threshold Level

Fast discrimination, a commonly used technique to detect pile-up, consists of splitting the incoming signal into two independent channels. The "fast" timing channel operates in parallel with the slower spectroscopic channel used to produce counts in the recorded spectrum. The trailing edge of the pulse from the fast channel triggers an inspection interval ($T_{Inspect}$), which is defined as GT x (RT + FT), where GT is the Guard Time multiplier constant holding a minimum and maximum value of 1.1 and 2.5, respectively. If a second pulse is detected by the fast channel within the $T_{Inspect}$ interval, it generates the *inhibit* signal, which prevents the ADC from processing the piled-up event and thus eliminating the convolved events. One of the important parameters of the fast discriminator is the threshold level, which sets the level such that only the pulses with amplitude greater or equal to the threshold will generate the inhibit signal to the linear gate [22]. Further details regarding pile-up rejection are presented in Section 4.5.

The fast discriminator circuit in the Osprey is capable of operating in manual mode, where the user can set the threshold level, or in auto mode, where the Osprey automatically sets the fast discriminator threshold level (FDisc) above an automatically determined system noise level. In manual mode, FDisc is set as a percentage value from 0 to 100, where 100 % approximately corresponds to 20 % of the full energy range of the MCA. In order to assess the impact of FDisc settings, several gamma-ray spectra were collected using $^{133}$Ba, $^{137}$Cs and $^{60}$Co at various thresholds. Table 5 lists the parameter settings used during this experiment.

**Table 5.** List of settings for Fast Discriminator assessment.

| Parameter | Setting |
|---|---|
| HV (volts) | 650 |
| Input count rate | Constant |
| Total observed count rate (kcps) | Variable due to FDisc setting<br>105 – 157 |
| Gain (Fine x Coarse) | 1.0 x 1.0 |
| Flat-top time (µs) | 0.5 |
| Rise-time (µs) | 1.0 |
| PUR Guard Time interval | 1.1x |
| LTC | Off |
| BLR mode | Auto |
| Fdisc setting | Variable |
| Fdisc shaping | Normal |

Figure 14 shows gamma-ray spectra measured at various FDisc threshold levels. At lower FDisc thresholds (<= 0.2 %), a significant reduction in the magnitude of the $^{133}$Ba photo-peaks (top-left, Figure 14) is seen. Since even very low amplitude noise pulses are able to trigger the *inhibit* signal, the system is prevented from accepting a large fraction of the input pulses and the overall count rate decreases. The higher count rate, lower-energy regions (corresponding to $^{133}$Ba peaks) of the spectrum are more

susceptible to this phenomenon. As the FDisc threshold level increases (top-right, Figure 14), the low amplitude noise no longer triggers the *inhibit* signal and therefore, fewer pulses are rejected and the overall count rate increases. For threshold levels between 0.5 % and 5.0 % there is minimal impact on the key peaks in the spectra above 200-keV, but the 80-keV from $^{133}$Ba is impacted since some of those events are now below the FDisc threshold. For FDisc values greater than 5%, incremental reductions in the peaks from lower to higher energies are seen.

The data and interpretation on FDisc indicate that values below 0.5% and above 5% can produce count rate distortions in the peak energies of interest. This effect is most notable for very low thresholds where variable system noise levels can have a major impact. To guard against systematic uncertainties that could be introduced by a combination of fixed threshold but variable instrument noise levels, the *auto* mode was selected for the field trial. Per Canberra documentation and the testing performed here, this should ensure that the FDisc threshold is always above the system noise level (a minimum of 3 % in *auto* mode). This is attractive for the UCVS field trial since it is performed outdoors over a long time period, making noise variations more likely.

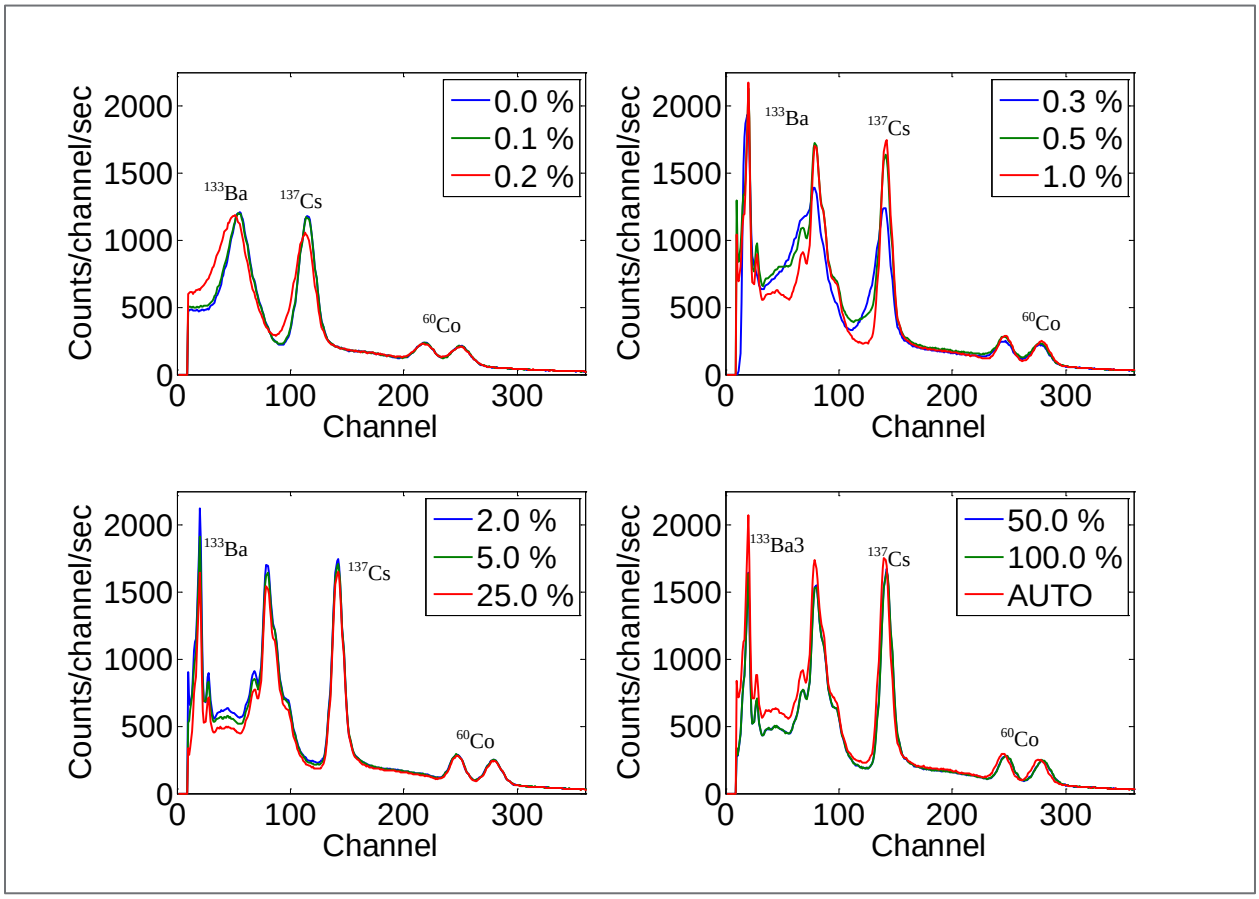


**Figure 14.** Gamma-ray spectra at various FDisc thresholds.

## 4.4 Time Segmentation Effects

The HEVA system, as part of a UCVS, is to be operated in a continuous, unattended mode during the field trial. Pulse height analysis (PHA) spectra will be collected for a set amount of real time and multiple spectra will be assembled into an aggregate spectrum for analysis as a single occupancy. While five minutes is the nominal occupancy period defined in the UCVS User Requirements [5], there are several reasons why a fixed acquisition time of five minutes is not appropriate for the field trial and subsequent analysis. One of those reasons is depicted in Figure 15 where a cylinder is placed on the UCVS in the middle of an ongoing acquisition. Avoiding this situation would require the operator to wait for the current acquisition run to be completed before placing the cylinder on the UCVS—an extra, undesirable burden on operations at WFFF.

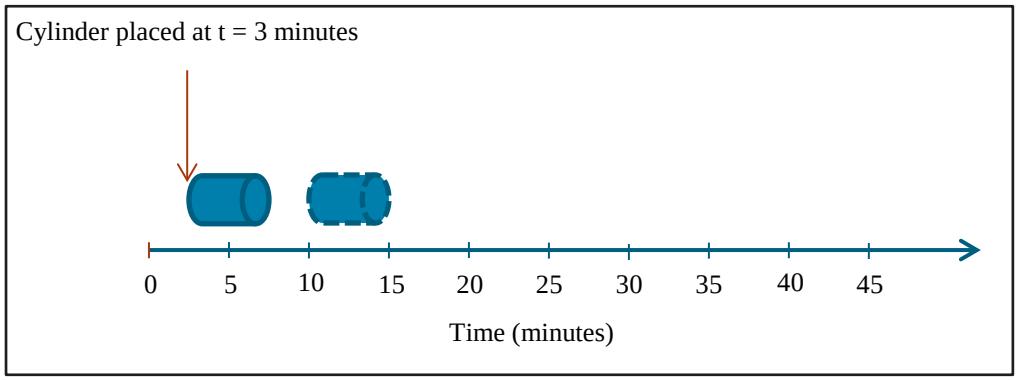


**Figure 15.** Sequence of events encountered during a cylinder measurement.

In general, shorter time segmentation is desired for flexibility in facility operations and post processing analysis. For example, it may be advantageous to analyze occupancies of less than five minutes. But short acquisition intervals can create issues with file number and size--smaller time segments requires more disk storage. In addition, there is a small amount of dead-time associated with buffering and writing files to disk. It was therefore decided to consider PHA acquisition times between 10 and 600 seconds. A total “occupancy” period of 600 seconds was collected using these PHA acquisition intervals of 10, 20, 30, 60, 150, 300 and 600 seconds long (real-time). For example, a set of 60 spectra were recorded at 10 seconds each, and a set of 10 spectra at 60 each seconds each. This procedure was repeated for count rates between 20 and 95 kcps.

Figures 16-20 show the observed 662-keV peak count rate and associated total live time for various total input count rates. Since the source-detector geometry is unchanged for all of the data points, the theoretical (and ideal) behavior would be that the peak count rate and live time values are identical for all values of PHA acquisition time. As those figures illustrate, however, that is definitely not the case. Instead, the average peak count rate decreases as the PHA acquisition time increases, eventually approaching the true average. These results correlate with the fact that the aggregated detector live-time is higher for the smaller time-segment data sets. For example, the total live-time associated with the 10-second interval is higher than 20-second interval. The Osprey appears to have an increasing positive bias in absolute count rate as the PHA acquisition interval decreases. The cause of the bias is unknown; however the very predictable trend is that the bias drops exponentially as the PHA acquisition interval increases. Table 6 contains the parameter settings used for these experiments.

**Table 6.** List of settings for the assessment of PHA acquisition times.

| Parameter | Setting |
|---|---|
| HV (volts) | 650 |
| Input count rate | Variable |
| Total observed count rate (kcps) | 20- 95 kcps |
| Gain (Fine x Coarse) | 1.0 x 1.0 |
| Flat-top time (µs) | 0.5 |
| Rise-time (µs) | 1.0 |
| PUR Guard Time interval | 2.5x |
| LTC | On |
| BLR mode | Auto |
| Fdisc setting | Auto |
| Fdisc shaping | Normal |

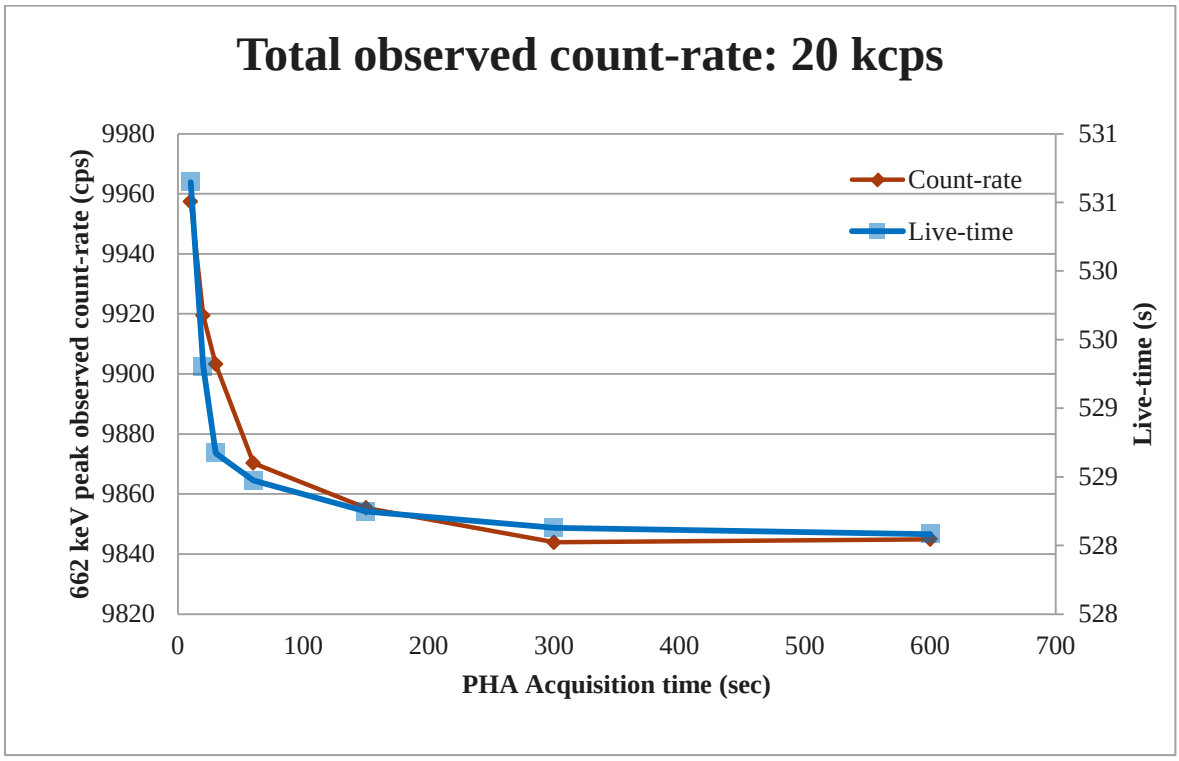


**Figure 16.** Peak count rate and the associated live-time at various PHA acquisition times at an observed total count rate of 20 kcps.

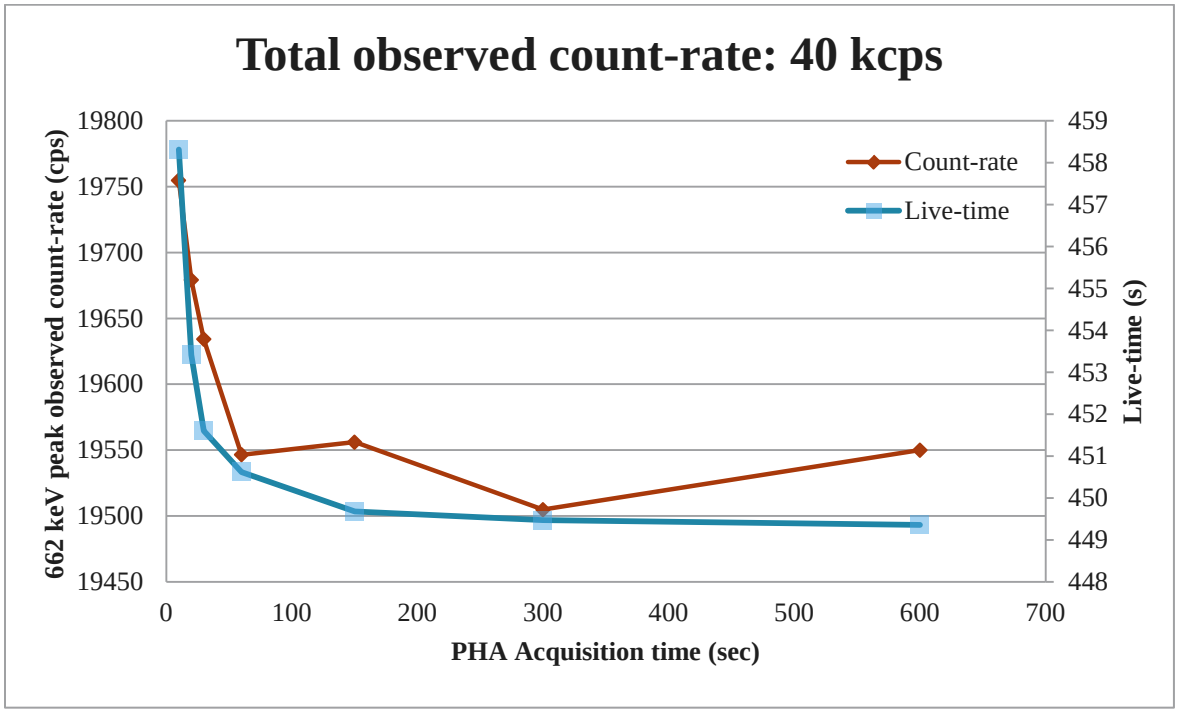


**Figure 17.** Peak count rate and the associated live-time at various PHA acquisition times at an observed total count rate of 40 kcps.

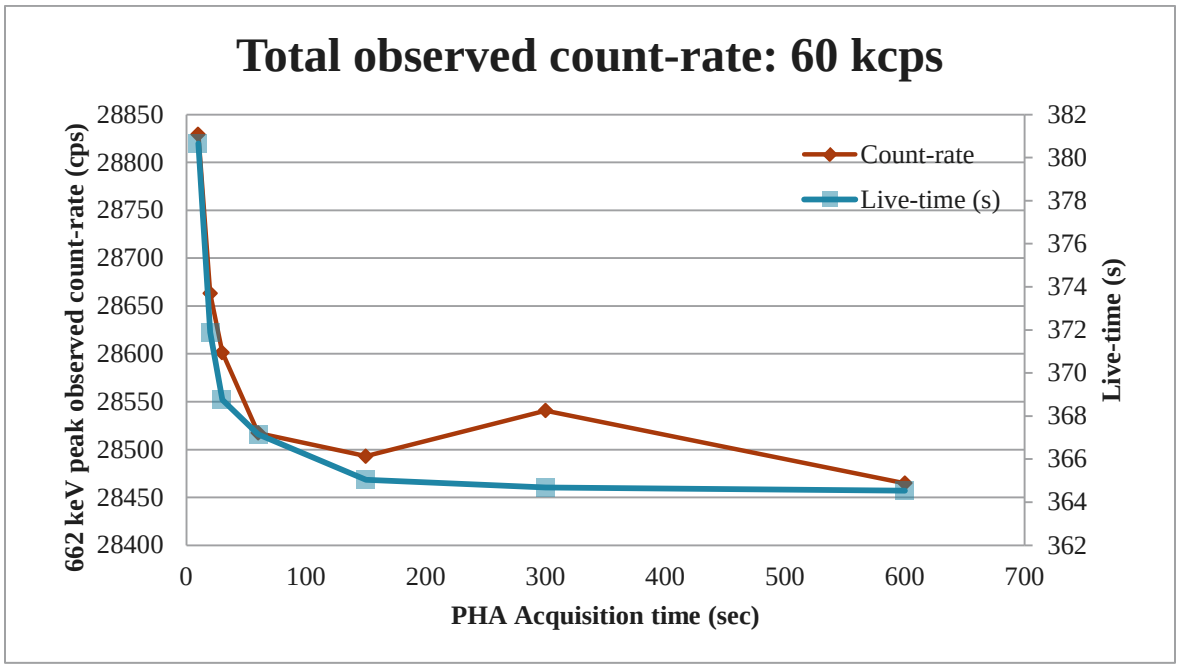


**Figure 18.** Peak count rate and the associated live-time at various PHA acquisition times at an observed total count rate of 60 kcps.

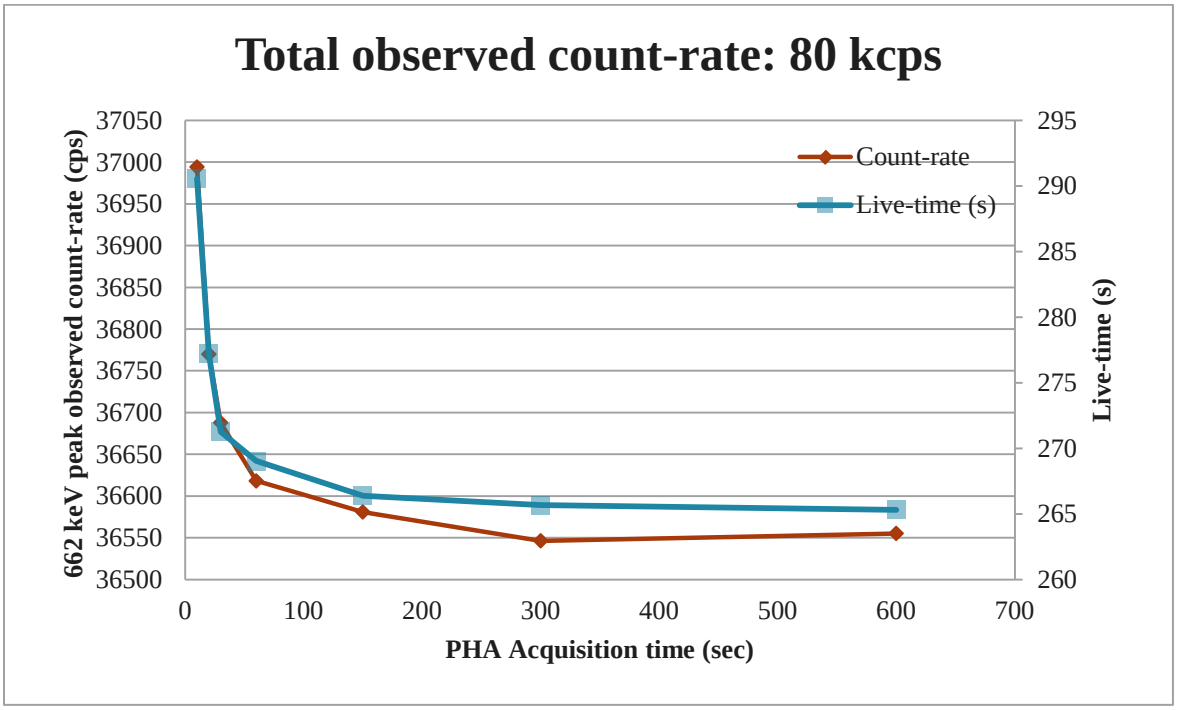


**Figure 19.** Peak count rate and the associated live-time at various PHA acquisition times at an observed total count rate of 80 kcps.

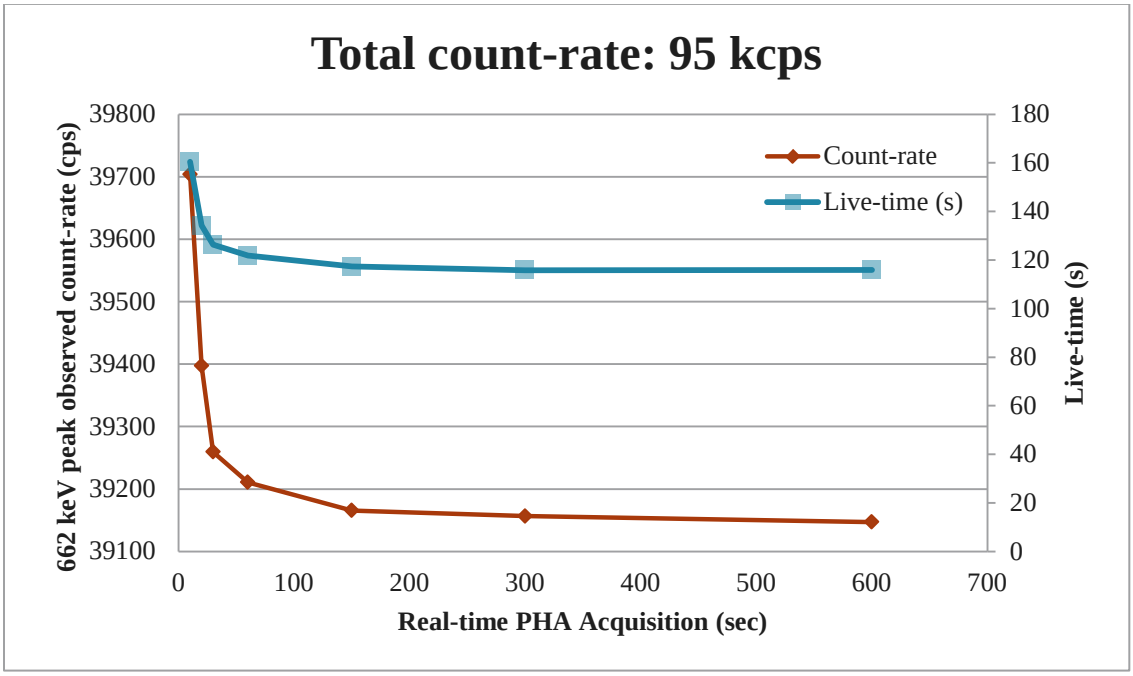


**Figure 20.** Peak count rate and the associated live-time various PHA acquisition times at an observed total count rate of 95 kcps.

Table 7 below shows the relative difference in peak count rate, as a function of PHA acquisition time and total input count rate. Fortunately, the data indicates that the bias in the peak count rate is relatively consistent across all input count rates. For the UCVS scenario, this means that a cylinder with heavy wall deposits will produce the same relative bias as a cylinder with the same enrichment but lower wall deposits. Therefore, the possibility exists to correct the relative bias, if that was needed for absolute calibration.

Based on the analysis presented here, and expectations of WFFF facility operations during the field trial, a PHA acquisition time of one minute was selected by PNNL. This value strikes an appropriate balance between the count rate bias (~ 0.2 %) from the average "true" count rate, and number of files per occupancy.

**Table 7.** Relative error in peak count rate as a function of PHA acquisition time and total input count rate, assuming a total "occupancy" duration of 600 seconds (real time)

| | **20 kcps** | **40 kcps** | **60 kcps** | **80 kcps** | **95 kcps** |
|---|---|---|---|---|---|
| **PHA time (sec)** | | | | | |
| **10** | -1.143% | -1.048% | -1.281% | -1.201% | -1.422% |
| **20** | -0.756% | -0.661% | -0.697% | -0.588% | -0.638% |
| **30** | -0.592% | -0.431% | -0.480% | -0.363% | -0.286% |
| **60** | -0.257% | 0.018% | -0.185% | -0.173% | -0.162% |
| **150** | -0.106% | -0.031% | -0.099% | -0.070% | -0.047% |
| **300** | 0.011% | 0.231% | -0.266% | 0.024% | -0.024% |
| **600** | 0.000% | 0.000% | 0.000% | 0.000% | 0.000% |

## 4.5 Pile-up Rejection Guard inspection interval (PUR Guard)

Pulse pile-up can result in an unexpected loss in counts in the photopeak along with the emergence of unexpected peaks, resulting from the pile-up and summing effects in a gamma-ray spectrum recorded at high counting rate. The Osprey includes a pulse pile-up rejection (PUR) method along with the live-time correction. The pile-up rejection in an Osprey is a function of the trapezoidal filter shaping constants, i.e. the RT and the FT, and the pile-up Guard Time (GT) coefficient. These three parameters together define the pile-up rejection interval, which is given by: pile-up rejection interval = GT x (RT + FT). The GT coefficient value ranges from 1.1 to 2.5 in steps of 0.1. The PUR rejection interval is triggered as soon as a pulse is detected in the fast shaping channel (fast discriminator). If a second pulse is detected within the time period of the rejection interval, it is considered as a piled-up event and the two pulses are rejected. Figure 21depicts the pile-up rejection scenario in an Osprey. The Osprey also adjusts the dead-time associated with the piled-up events by performing a Live Time Correction (LTC). PUR LTC can be toggled on and off.

Figure 21 shows the pileup rejection scenario in an Osprey. Note that the pile-up GT is set to 1.1x (minimum allowed by the Osprey) and the vertical dotted line marks the end of the PUR interval. When a pulse above the fast discriminator threshold is detected in the fast channel, a pileup rejection interval, or inspection interval ($T_{inspect}$), is generated. This event is triggered with the rising edge of the fast channel output. In parallel, the slow channel performs its normal pulse processing routine. Should another pulse

arrive within the inspection interval, the fast discriminator will detect this event as a pileup and the two pulses will be thus rejected from being processed by the slow channel. The pile-up rejection process behaves similarly at different pile-up GT settings. For example, when the pile-up GT is set to 2.5x (maximum allowed by the Osprey), the PUR interval is extended until the initial pulse has fully returned to the baseline. A higher GT allows for maximum pile-up rejection; however it can also result in decreased throughput. Therefore, it is important to determine a suitable GT according to the given operating conditions, mainly the expected maximum count rate and the shaping filter parameters.

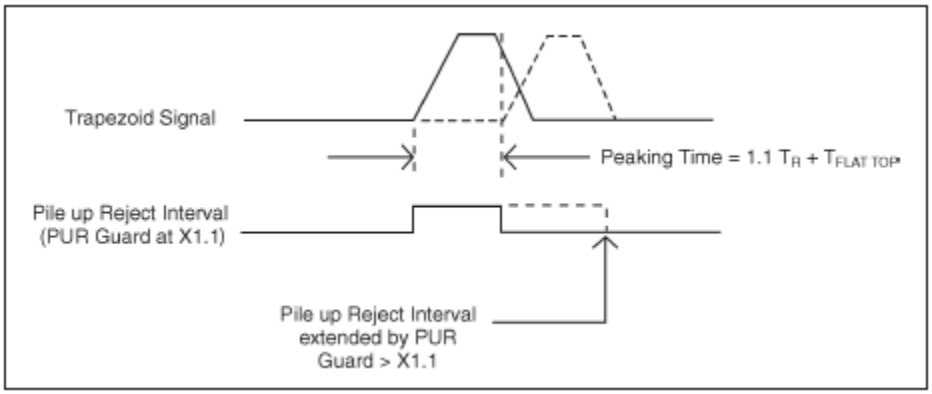


**Figure 21.** Pile-up rejection scenario in an Osprey [18].

Evaluation of the PUR settings were performed using a series of $^{137}$Cs gamma-ray spectra collected at various GT values while holding all other variables constant, including the input count rate (input count rate > 160 kcps).Table 8 contains the other parameter settings used for the experiments in this section.

**Table 8.** List of settings for PUR assessment.

| Parameter | Setting |
|---|---|
| HV (volts) | 682 |
| Input count rate | Constant |
| Total observed count rate (kcps) | 88 kcps to 102 kcps (due to variable pile-up guard) |
| Gain (Fine x Coarse) | 1.0 x 1.0 |
| Flat-top time (μs) | 0.5 |
| Rise-time (μs) | 1.0 |
| PUR Guard Time interval | Variable from 1.1x to 2.5x |
| LTC | On |
| BLR mode | Auto |
| Fdisc setting | Auto |
| Fdisc shaping | Normal |

The figure below shows the comparison between $^{137}$Cs gamma-ray spectra recorded at various PUR GT multiplier settings. With the PUR LTC disabled, regardless of the PUR GT value, the Osprey performs no pile-up rejection, which results in higher overall count rates and more spectral features associated with pileup, including the sum peak, the Compton continuum between the primary and sum peaks, and degraded peak energy resolution in the primary peak (the green and cyan lines overlap). With the PUR LTC enabled and the GT value set to 1.1, the reduction in pileup effects is evident: The 662-keV peak stands out more sharply against the continuum as the pile-up around the peak is reduced and the continuum between the photopeak and the sum peak and intervening continuum are reduced significantly. With the GT value set to a maximum of 2.5, even further reduction is observed, however, the area under the 662-keV photopeak also decreases—the signal of interest is reduced. Note that the GT setting of 2.5 does not completely eliminate the summing features because some of those pulses still arrive within the resolving time of the fast channel due to the very high input count rates. This phenomenon is also known as chance coincidence [20].

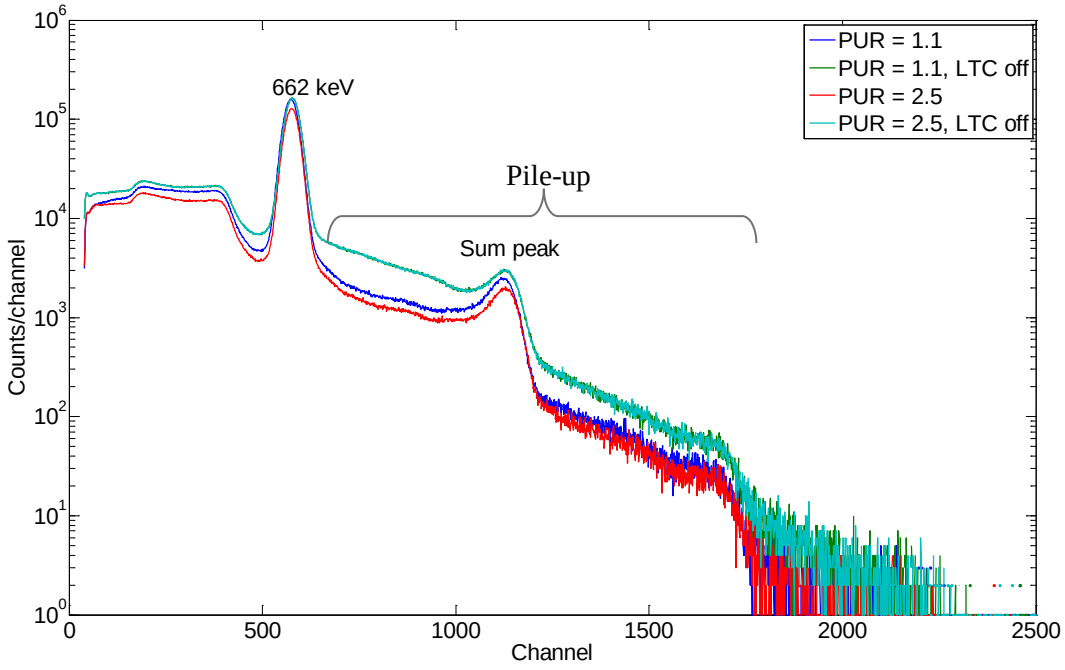


**Figure 22.** Comparison of $^{137}$Cs spectra at various PUR Guard Time intervals.

Table 9 provides a numerical summary of the counts from various ROIs of the gamma-ray spectra (180 seconds real-time) collected over a range of PUR GT multiplier values. Here, the term *Total Counts* refers to the gross sum of counts across the full MCA range, *662-keV Peak Counts* refers to the net counts under the peak after fitting and subtracting the underlying continuum, *Compton Continuum* refers to the counts under the ROI spanning from the backscatter peak (184-keV) to the Compton edge (477-keV) corresponding to the 662-keV peak and *Pileup Counts* refers to the sum of counts beyond the 662-keV peak (+/- three sigma about the centroid). The "% change" column represents the change in counts with respect to the case where PUR/LTC is disabled.

**Table 9.** Tabular comparison of the spectral features of the gamma-ray spectra recorded at various PUR GT multiplier values.

| PUR GT | Total Counts | % Change |
|---|---|---|
| Disabled | 18480016 | NA |
| 1.1 | 15835416 | 14.31% |
| 1.3 | 15498260 | 16.14% |
| 1.5 | 15100812 | 18.29% |
| 1.7 | 14715944 | 20.37% |
| 1.9 | 14281874 | 22.72% |
| 2.1 | 13870525 | 24.94% |
| 2.3 | 13435229 | 27.30% |
| 2.5 | 13002623 | 29.64% |

| PUR GT | 662-keV Peak Counts | % Change |
|---|---|---|
| Disabled | 7391056 | NA |
| 1.1 | 7147842 | 3.29% |
| 1.3 | 6959152 | 5.84% |
| 1.5 | 6731214 | 8.93% |
| 1.7 | 6530404 | 11.64% |
| 1.9 | 6295038 | 14.83% |
| 2.1 | 6119871 | 17.20% |
| 2.3 | 5920615 | 19.89% |
| 2.5 | 5709668 | 22.75% |

| PUR GT | Compton Continuum | % Change |
|---|---|---|
| Disabled | 7010580 | NA |
| 1.1 | 6103765 | 12.93% |
| 1.3 | 6032150 | 13.96% |
| 1.5 | 5909456 | 15.71% |
| 1.7 | 5770152 | 17.69% |
| 1.9 | 5598643 | 20.14% |
| 2.1 | 5435631 | 22.47% |
| 2.3 | 5256793 | 25.02% |
| 2.5 | 5080460 | 27.53% |

| PUR GT | Pile-up Counts | % Change |
|---|---|---|
| Disabled | 1685320 | NA |
| 1.1 | 892410 | 47.05% |
| 1.3 | 868541 | 48.46% |
| 1.5 | 840714 | 50.12% |
| 1.7 | 817931 | 51.47% |
| 1.9 | 791117 | 53.06% |
| 2.1 | 767020 | 54.49% |
| 2.3 | 741986 | 55.97% |
| 2.5 | 718813 | 57.35% |

The data of Table 9 indicates that a reduction in the summing features must be balanced by a reduction in the signal of interest, in this case the 662-keV photopeak. For these experiments, a GT value of 2.5 reduces the 662-keV signal and the pile-up continuum by 22.75 % and 57.35 %, respectively. In the case of UCVS, the analogy would be a reduction in the 186, 765 and 1001-keV signals as the primary peaks, and the nontraditional signal from 3-10 MeV in the pileup region. Reductions in the magnitude of the primary peaks is not expected to be problematic since the counts under these photopeaks are present in abundance and the error governed by the Poisson counting statics is much smaller than the overall systematic uncertainty. But the impact of pileup events on the nontraditional signal could be problematic because the signal of interest is several orders of magnitude smaller than the primary peaks. It was deemed a priority, therefore, to reduce false counts in the nontraditional assay portion of the spectrum from 3-8 MeV to the extent practicable. Based on this analysis and interpretation a maximum GT coefficient of 2.5 was adopted for the UCVS field trial.

## 4.6 LTC verification

Most gamma-ray spectroscopy systems are equipped with a live-time correction (LTC) mechanism, where the system keeps track of the time interval for which the detector did not exhibit any dead-time due to the pulse pile-up and pulse processing. Generally speaking, live-time correction mechanisms are accurate only over a specified range of count rates. Therefore, it was important to verify that the Osprey LTC method is accurate over the expected range of HEVA count rates in the UCVS scenario. According to the manufacturer's specification, the LTC in an Osprey is expected to be accurate within 5% for the count rates ranging up to 50 kcps [21]. As described previously, certain cylinders may present count rates above this rate and therefore, it is necessary to verify the accuracy of the LTC at these count rates.

The LTC performance can be measured using a two-source method (adapted from [18]) in which a reference source is used to produce a baseline count rate between 3 and 5 kcps. The distance between the reference source and the detector is kept constant after achieving the target count rate. The LTC must then be turned on and the system should be configured to record the counts for a prescribed length of *live-time*, typically between 300 to 600 seconds. After collecting the reference spectra, another source, which is a different isotope from the reference source, is moved near the detector to increase the count rate in regions well separated from the reference photopeak. The goal is to monitor the net area under the reference photopeak in the presence of another source. In theory (and if LTC methods are perfect), the net area of the reference peak will remain constant regardless of the spectral contributions from the additional source. See Figure 23 for the setup schematic.

For the purpose of verifying the LTC accuracy of the Osprey, the above mentioned method was conducted using $^{137}$Cs and $^{57}$Co sources and the same setting described in Table 8. The 662-keV photopeak is taken as the reference peak and $^{57}$Co is treated as the secondary, or background source. Note that all $^{57}$Co contributions are well below the 662-keV peak and therefore, cannot contribute to the 662-keV peak, even via pileup events. Table 10 provides a summary of the results from this test.

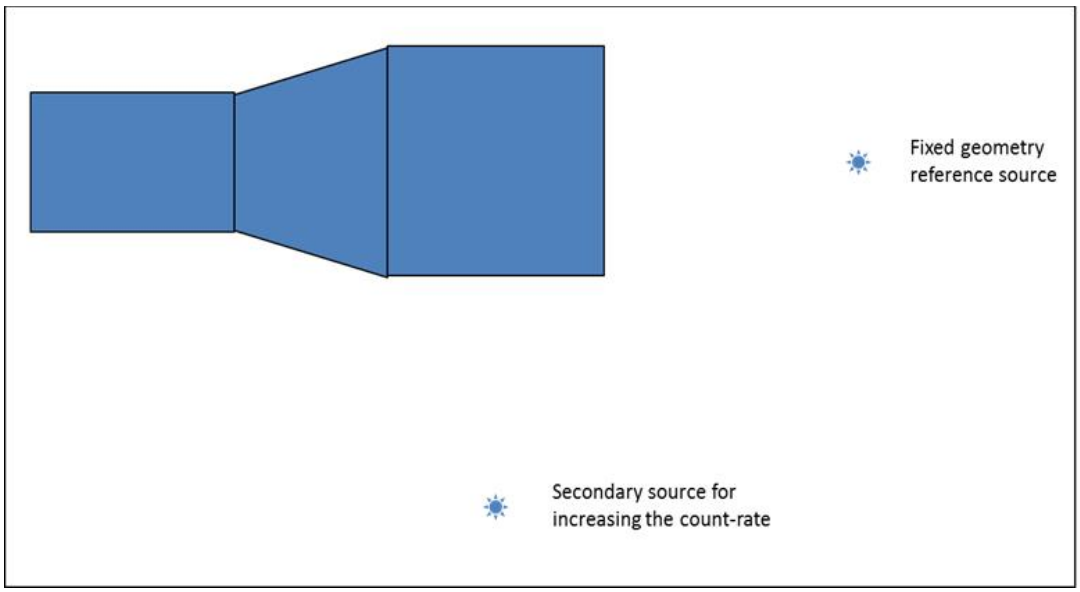


**Figure 23.** Source-detector geometry setup for the LTC verification experiment.

**Table 10.** LTC accuracy verification using $^{137}$Cs and $^{57}$Co.

| Source | Approx. count rate (kcps) | 662-keV net peak area (counts) | Accuracy (%) |
|---|---|---|---|
| $^{137}$Cs | 3 | 692756 | NA |
| $^{137}$Cs + $^{57}$Co | 10 | 696479 | 0.54 |
| $^{137}$Cs + $^{57}$Co | 20 | 694626 | 0.27 |
| $^{137}$Cs + $^{57}$Co | 30 | 697017 | 0.62 |
| $^{137}$Cs + $^{57}$Co | 40 | 704787 | 1.74 |
| $^{137}$Cs + $^{57}$Co | 50 | 703989 | 1.62 |

The results indicate that the Osprey LTC accuracy is actually lower than the stated limit of 5% up to a total input count rate of approximately 50 kcps. That said, systematic errors on the order of 2% could be a significant factor in HEVA analysis where total uncertainties are expected to be in the range of 3-4% for the traditional and nontraditional signals. Therefore, the effect of the LTC should be mitigated by maintaining input count rates below approximately 30 kcps. While very conservative simulation assumptions for wall deposits indicate that HEVA may see count rates greater than 50 kcps on some cylinders, it remains to be seen whether that is actually the case for measured cylinders with the new HEVA module design.

# 5.0 Neutron Efficiency Benchmark

## 5.1 Overview

HEVA's nontraditional signal can be viewed as an indirect totals neutron detector and as such, it is important to quantify the intrinsic neutron detection efficiency of the HEVA module. For HEVA, the intrinsic neutron efficiency is interpreted as the total number of gamma-ray counts in the non-traditional ROI (approximately 3-8.5 MeV) per incident neutron, and can be calculated as

$$R = \varepsilon_{int}\varepsilon_{geo}A \qquad (0.1)$$

where, $R$ is the live-time corrected count rate (total counts / time) in the non-traditional ROI, $\varepsilon_{int}$ is the intrinsic neutron efficiency, $\varepsilon_{geo}$ is the geometric efficiency and $A$ is the neutron emission rate. It is important to note that the geometric efficiency, $\varepsilon_{geo}$, is calculated with respect to the entire front face of the collimator assembly (rather than just the detector surface), since the collimator acts as a neutron converter by emitting prompt gamma-rays upon neutron capture. The geometric efficiency parameter is calculated as follows:

$$\varepsilon_{geo} = \frac{\Omega}{4\pi} = \frac{1}{2}\left(1 - \frac{d^2}{\sqrt{d^2 + a^2}}\right) \qquad (0.2)$$

where, $d$ is the source-detector standoff distance and $a$ is the radius of the collimator. It is expected that the majority of the non-traditional signature comes from the activation of $^{56}$Fe and $^{127}$I. While previous modeling was informative regarding the relatively strengths of these two components [23], it is desirable that empirical support for these predictions be collected.

A key factor in the stability of the non-traditional signature is accurate definition of the 3-8.5 MeV ROI. The accuracy of the energy calibration is limited by the number of available photopeaks and the inherent non-linearity of the NaI detectors. Defining the lower boundary of the ROI is particularly important since more of the nontraditional signal is in the 3-5 MeV range than in the higher (6-8.5) energy range. Small changes in the lower boundary of the ROI can have significant effect on the assay precision. The sources used in the energy calibration for this experiment are shown below in Table 11.

**Table 11.** List of calibration sources and their respective photo-peak energies.

| Isotope/source reaction | $E_\gamma$ – Photo-peak energy (keV) |
|---|---|
| $^{133}$Ba | 81.0, 356.0 |
| $^{57}$Co | 122.1 |
| $^{22}$Na | 511.0, 1274.5 |
| $^{137}$Cs | 661.7 |
| $^{60}$Co | 1173.2, 1332.5 |
| $^{1}$H(n, γ)$^{2}$H | 2223.3 |
| Am-Be: α + $^{9}$Be → $^{13}$C$^{*}$ → $^{1}$n + $^{12}$ C + γ | 4438.9 |

One of the prototype HEVA detector modules intended for use in the UCVS field trial (see Figure 24) was used for this experiment. The measurement system consisted of a ø3″×3″ NaI(Tl) detector coupled to an Osprey digital MCA tube base. The detector was operated at 650 volts with the gain (fine × coarse) set to unity and the trapezoidal filter rise time and flat-top times set to 1.0 and 0.5 μs, respectively, consistent with the results presented earlier in this report.

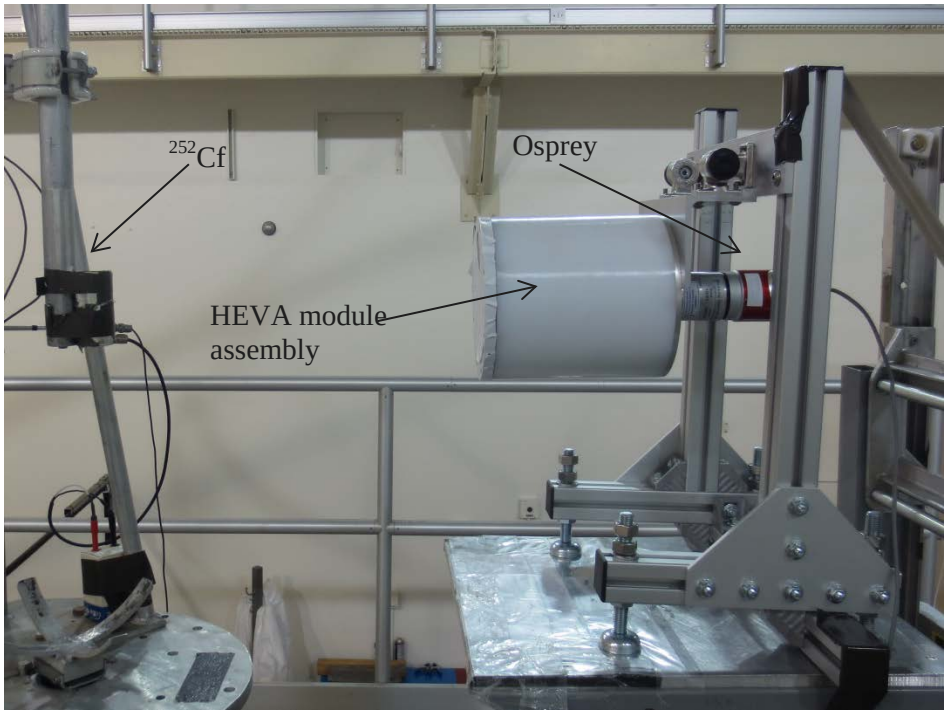


**Figure 24.** Experimental setup at a PNNL low-scatter neutron facility.

In order to obtain the prompt gamma-ray spectrum, a bare $^{252}$Cf neutron source, emitting $1.5\times10^{7}$ neutrons per second, was placed 35-cm away from the detector. Note that this is roughly two orders of magnitude greater than the expected neutron emission rate from a 5 wt% Type 30B $UF_6$ cylinder. A 5.1-cm thick lead brick (not pictured) was placed in between the source and the detector to attenuate the majority of the fission and direct-decay gamma-rays. For the purpose of investigating the contributions of the $^{56}$Fe prompt gamma-rays to the non-traditional signature, the same experiment was performed with the outer cylindrical steel collimator layers removed (except for the central steel assembly which is required to support the detector, see Figure 25).

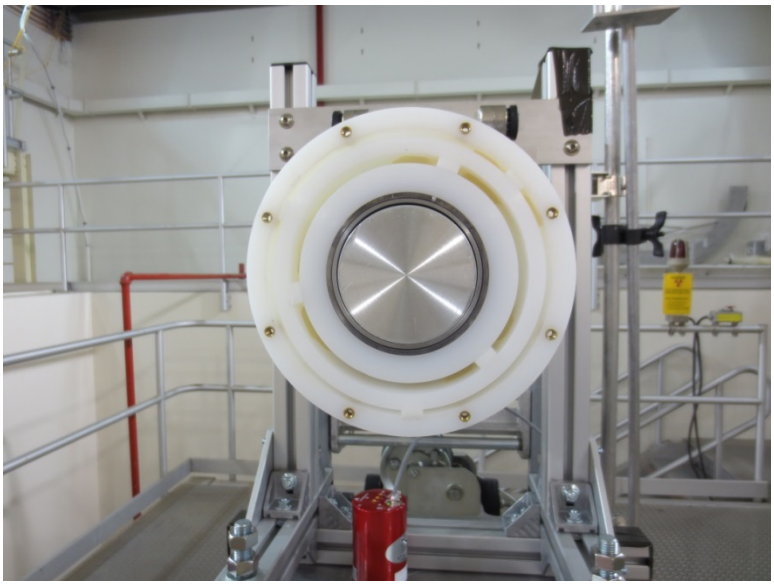

**Figure 25.** Front-view of the collimator assembly with the outer steel layers removed.

Figure 26 shows the net (background-subtracted) prompt gamma-ray count rate spectra obtained using the methods described earlier. The effect of the steel shells in the collimator is clearly visible. The photopeak near 7.64 MeV and escape peaks from neutron capture on $^{56}$Fe are significantly diminished when the steel layers are removed, and the net count rate in the non-traditional ROI (3 – 8.5 MeV) is greater by 97.3 cps with the extra steel layers in place. When the outer steel layers are not present, the majority of the high energy prompt gamma-rays are from the activation of the NaI(Tl) crystal, though some Fe contribution is still visible due to the structural material in and around the HEVA module.
Table 12 compares the intrinsic neutron efficiency for the two cases. The additional steel sleeves increase the intrinsic neutron efficiency by 7.75 %. These results are consistent with past modeling efforts which showed, for a previous HEVA collimator design, that the majority of the non-traditional signal is from the iodine in the detector (50.5%), followed by the thicker outer steel layer (24.6%), and then by the thin inner steel layer (16.3%) and a small amount from the cylinder wall and $UF_6$ [23]. The new HEVA design contains less steel to reduce the weight of each module, so we expect the relative contribution from the outer steel layers to be smaller than the previous design. The new design maintains the desired intensity of the non-traditional signal, with lower overall mass and improved modularity.

A closer look at the spectra in Figure 26 reveals the fact that a larger fraction of the prompt gamma contributions from iron is within the 6 – 8.5 MeV ROI. The majority of the intense emissions above 6.0 MeV correspond to the photo-peaks at 7.278, 7.631 and 7.645 MeV. Therefore, the main effect of including steel in the collimator can be evaluated by comparing the count rate in the 6.0 – 8.5 MeV region. The reason for selecting 6.0 MeV as the lower limit of the ROI is to capture any escape peaks that may originate from the pair-production reaction at high energies. Figure 26 below shows the result of including steel in the HEVA collimator. The intrinsic neutron efficiency under 6 – 8.5 MeV ROI is much lower than the 3 – 8.5 MeV ROI due to the obvious reduction in the number of counts. However, by this metric the intrinsic neutron efficiency increases by 38.5 % when the steel layers are added.

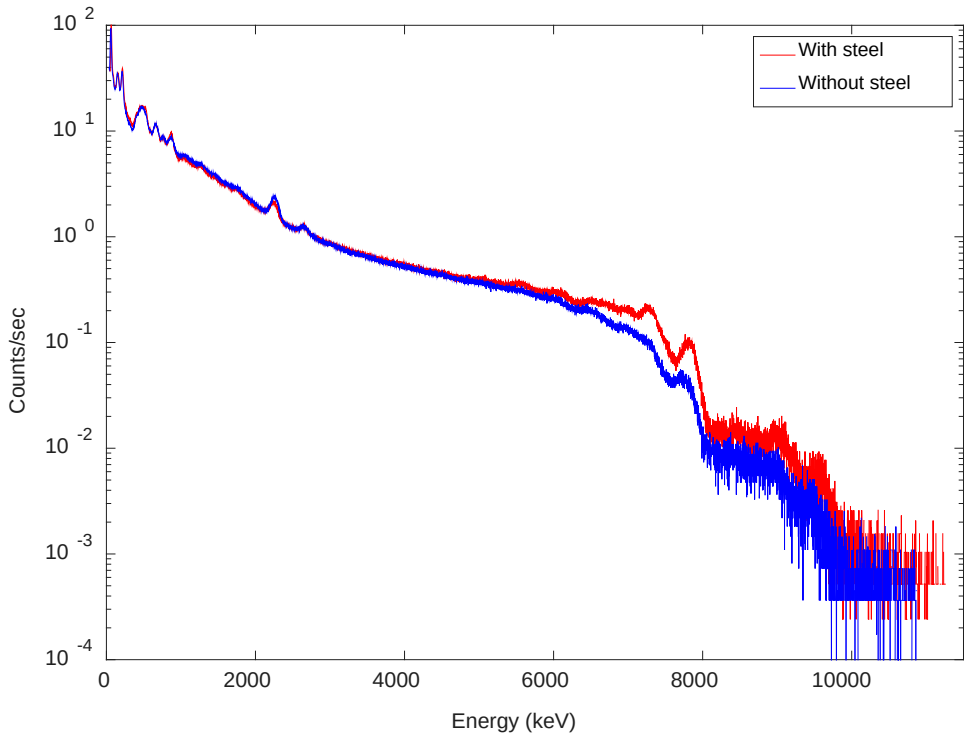


**Figure 26.** Comparison of the gamma-ray spectra measured with and without steel in the collimator.

**Table 12.** Intrinsic neutron efficiency for 3 to 8.5 MeV ROI.

| | **All Steel Layers** | **No Outer Steel Layers** |
|---|---|---|
| **3 – 8.5 MeV ROI Counts-rate (cps)** | 1362.5 | 1265.2 |
| **Distance (d, cm)** | 35 | 35 |
| **Collimator radius (a, cm)** | 9.7 | 9.7 |
| **Source Activity (neutrons per sec)** | $1.5 \times 10^7$ | $1.5 \times 10^7$ |
| **Geometric Eff. ($\varepsilon_{geo}$)** | 0.01816 | 0.01816 |
| **Intrinsic Eff. ($\varepsilon_{int}$) (%)** | 0.500 | 0.464 |

**Table 13.** Intrinsic neutron efficiency, for 6.0 to 8.5 MeV ROI, using the same test configuration of Table 12.

| | **All Steel Layers** | **No Outer Steel Layers** |
|---|---|---|
| **6 – 8.5 MeV ROI Counts-rate (cps)** | 268.1 | 193.5 |
| **Geometric Eff. ($\varepsilon_{geo}$)** | 0.01816 | 0.01816 |
| **Intrinsic Eff. ($\varepsilon_{int}$) (%)** | 0.098 | 0.071 |

The reliability of different energy calibration approaches was then investigated. A 3-point calibration method was assumed because it is expected that only three well-resolved and intense lines are likely to be available for the spectra from each cylinder occupancy: 186-keV, 767-keV and 1001-keV. For this laboratory experiment, three peaks with similar energies were chosen as surrogates: 122.1-keV ($^{57}$Co), 661.7-keV ($^{137}$Cs) and 1173.2-keV ($^{60}$Co). Figure 27 shows the linear and quadratic calibration fit performed using these replacement photo-peak energies. Table 14 and Figure 28 provide tabular and graphical summaries of the relative error between true and calculated peak energies.

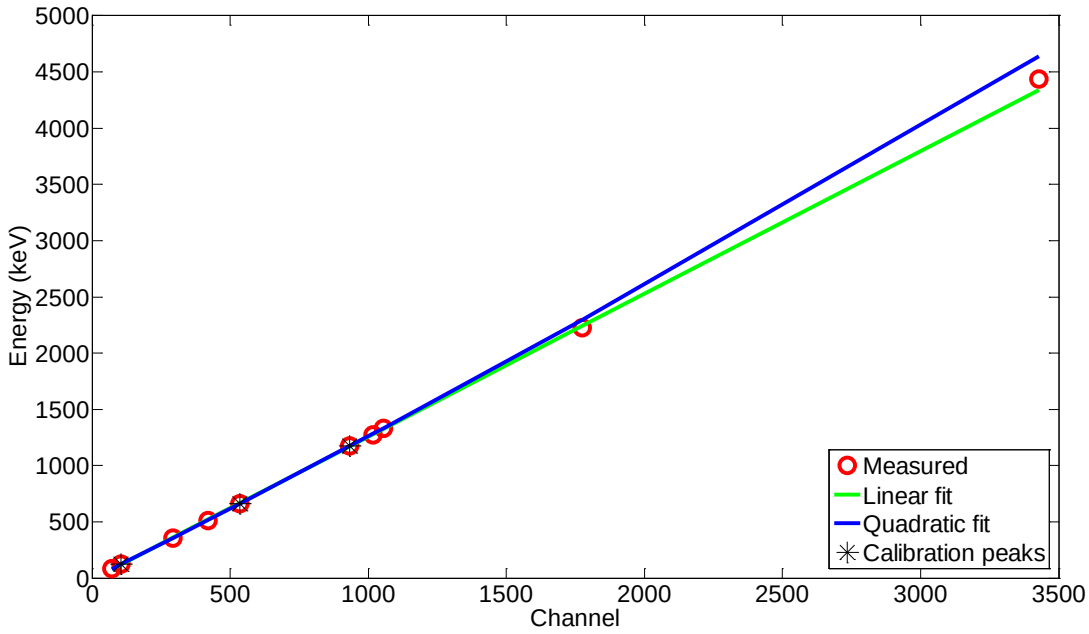


**Figure 27.** Linear and quadratic calibration fit using only three photo-peak energies

**Table 14.** Relative error associated with the linear and quadratic calibration fits.

| Photo-peak Energy (keV) | Linear calibration (keV) | Quadratic calibration (keV) | Relative Error – linear (%) | Relative Error – Quadratic (%) |
|---|---|---|---|---|
| 80.997 | 76.995 | 79.958 | 4.94 | 1.30 |
| 122.060 | 120.124 | 122.060 | 1.59 | 0.00 |
| 356.017 | 359.691 | 357.404 | -1.03 | -0.39 |
| 511.000 | 520.909 | 517.195 | -1.94 | -1.20 |
| 661.660 | 665.685 | 661.660 | -0.61 | 0.00 |
| 1173.240 | 1171.151 | 1173.240 | 0.18 | 0.00 |
| 1274.530 | 1277.736 | 1282.544 | -0.25 | -0.62 |
| 1332.460 | 1326.363 | 1332.576 | 0.46 | -0.01 |
| 2223.250 | 2240.993 | 2292.940 | -0.80 | -3.04 |
| 4438.910 | 4340.824 | 4636.419 | 2.21 | -4.26 |

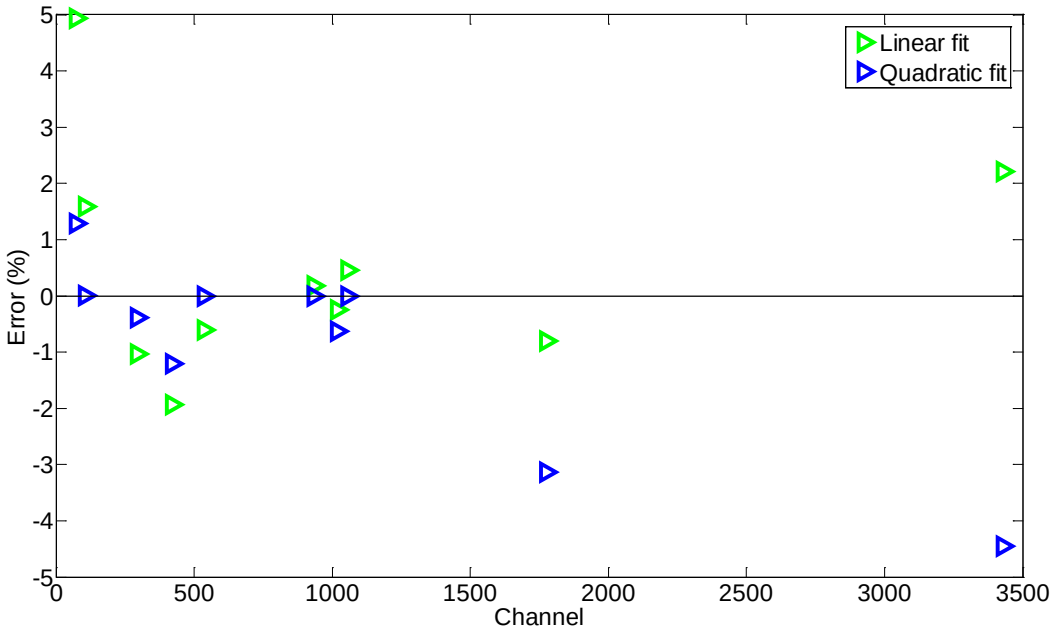


**Figure 28.** Relative error associated with the linear and the quadratic calibration fits

The relative errors associated with the linear fit are quite high at lower energies in comparison with the quadratic fit. This is due to the inherent non-linearity of NaI(Tl) [20]. However, it appears that for energies above approximately 1 MeV, a linear energy calibration may be more effective, and therefore, may be preferred for setting the lower boundary of the nontraditional ROI. Further investigation, using multiple detectors and larger data sets from a number of cylinder assays, is needed to more definitely assess the most appropriate functional form for energy calibration on the nontraditional ROI. This additional investigation will be performed as a part of the data analysis tasks associated with the field trial, using actual data from a large number of cylinders.

# 6.0 Detector Activation

Activation of the detector medium is a common problem faced during active-interrogation methods such as in Prompt Gamma Neutron Activation Analysis (PGNAA). Though the HEVA methods is completely passive, the relatively high total neutron fluence emitted by $UF_6$ cylinders and the desire to use the high-energy nontraditional ROI as a totals neutron signature means that the effects of activation need to be considered.

Upon neutron irradiation, the elements composing the detector medium may get activated and the subsequent decay radiation can interfere with the measurement of interest. Depending on the relative abundance of the target element, neutron absorption cross-section and half-life, some scintillator media can be more susceptible to such activation. NaI(Tl) is a material that fits most of the abovementioned criteria. The prompt gamma rays produced upon neutron irradiation are usually of high energies, up to 10 MeV. In order to capture such high energy gamma rays, a relatively large crystal is required (3×3, 5×5, etc.).

A large sodium iodide crystal is susceptible to this scenario where the reaction $^{127}I + {}^{1}n$ leads to the production of $^{128}I$, which undergoes beta minus decay to an excited state of $^{128}Xe$. The endpoint energy of this beta decay is 2.119 MeV and the subsequent de-excitation of $^{128}Xe$ to the ground state leads to the emission of a 442.9-keV gamma-ray [24]. The Na and I in sodium iodide have identical atom densities and therefore the amount of induced activity is governed by their respective neutron absorption cross-section and the half-lives of the activation products, i.e. $^{24}Na$ and $^{128}I$. Moreover, the production and decay of $^{128}I$ is the major contributor to the induced activity [24]. There are two primary reasons that this is the case:

1. In comparison to $^{23}Na$, $^{127}I$ has a considerably larger thermal and energy-averaged neutron absorption cross-section due the presence of an intense resonance between 10 eV to 10-keV. This leads to a much higher production of $^{128}I$ than $^{24}Na$. Figure 29 depicts this comparison.
2. $^{128}I$ (~24.99 minutes) has a shorter half-life as compared to $^{24}Na$ (~ 894 minutes) and therefore presents a greater activity per number of atoms created.

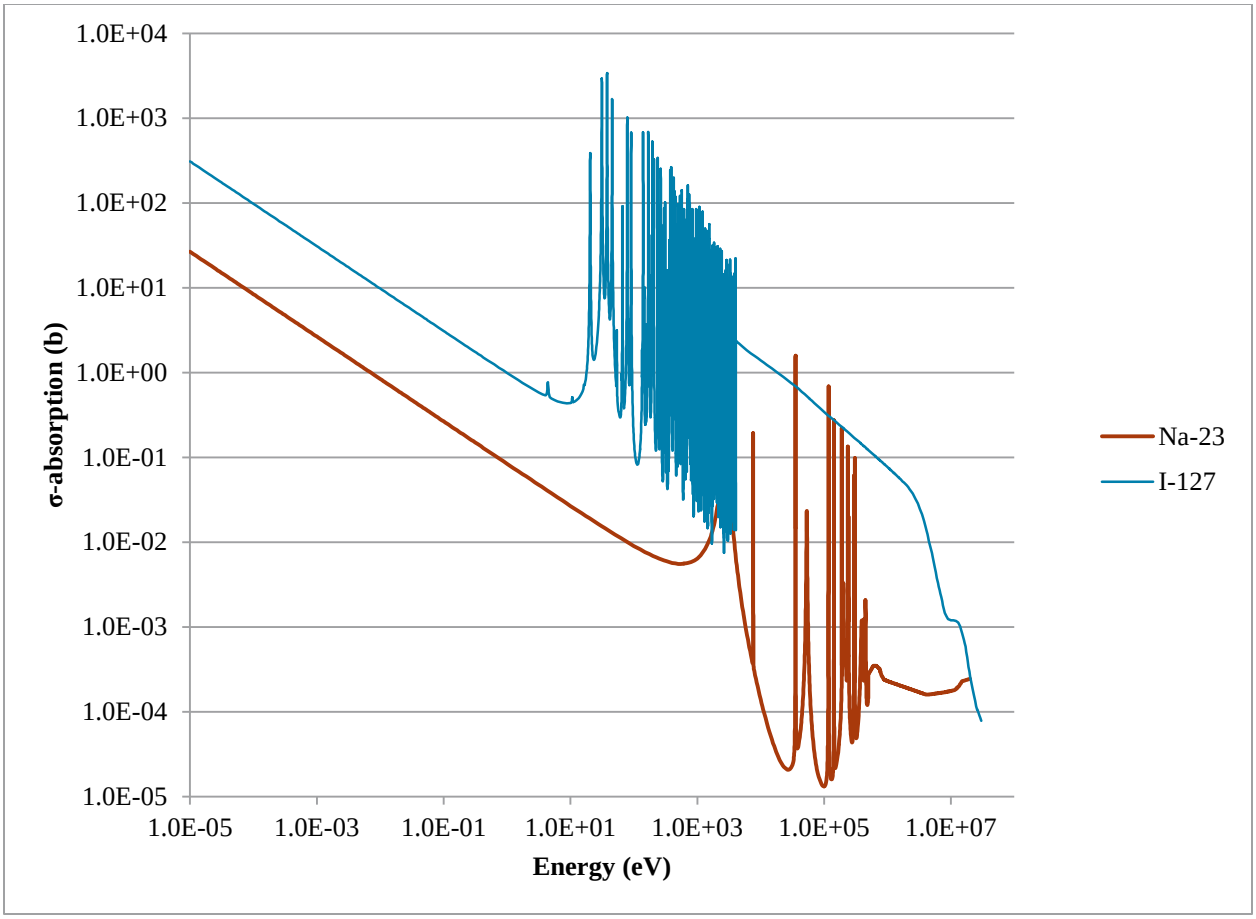


**Figure 29.** Comparison of neutron absorption cross-sections (from ENDF VII.1).

As mentioned earlier, the neutron source term in the UCVS scenario is comprised of neutrons from the reaction $^{19}F(\alpha, n)\ ^{22}Na$, spontaneous fission of $^{238}U$ and from induced fission. These neutrons can interact with the NaI crystal and produce $^{128}I$ via the above mentioned mechanism. PNNL defined an experiment to better understand the yield and anticipated impact of the activation signatures for HEVA modules in the cylinder assay scenario. The same test configuration described earlier for the intrinsic neutron efficiency study was utilized here. Note that because these tests used a $^{252}Cf$ source, the interrogating neutron spectrum is different than would be emitted by a $UF_6$ cylinder (especially a product cylinder). The average neutron energy for the $^{19}F(\alpha, n)$ is less than 1.2 MeV and for $^{252}Cf$ it is 2.14 MeV. Since the dominant neutron source from a cylinder is from $^{19}F(\alpha,n)$, the neutron fluence is somewhat considerably "softer" than that from $^{252}Cf$ used in this study, which would affect the neutron moderation and capture rate.

Measurements were performed before and after exposing the detector to the neutron source. Figure 30 shows the comparison of these spectra. The post-irradiation spectrum was collected for 300 seconds (real-time) and it clearly shows the evidence of the activation of $^{127}I$ to $^{128}I$. The post-irradiation count rate increased from 124 cps to 1797 cps. The vast majority of that additional count rate, as shown in Figure 30, is in the continuum extending to approximately 2 MeV. This continuum is consistent with the expected behavior from beta emission in 128I. More quantitatively, the calculated endpoint energy for the

continuum shown in red is ~2155-keV, consistent with the published beta endpoint energy of 2119-keV. Based on these results, it is assumed that the production of $^{24}$Na is negligible in the HEVA detectors.

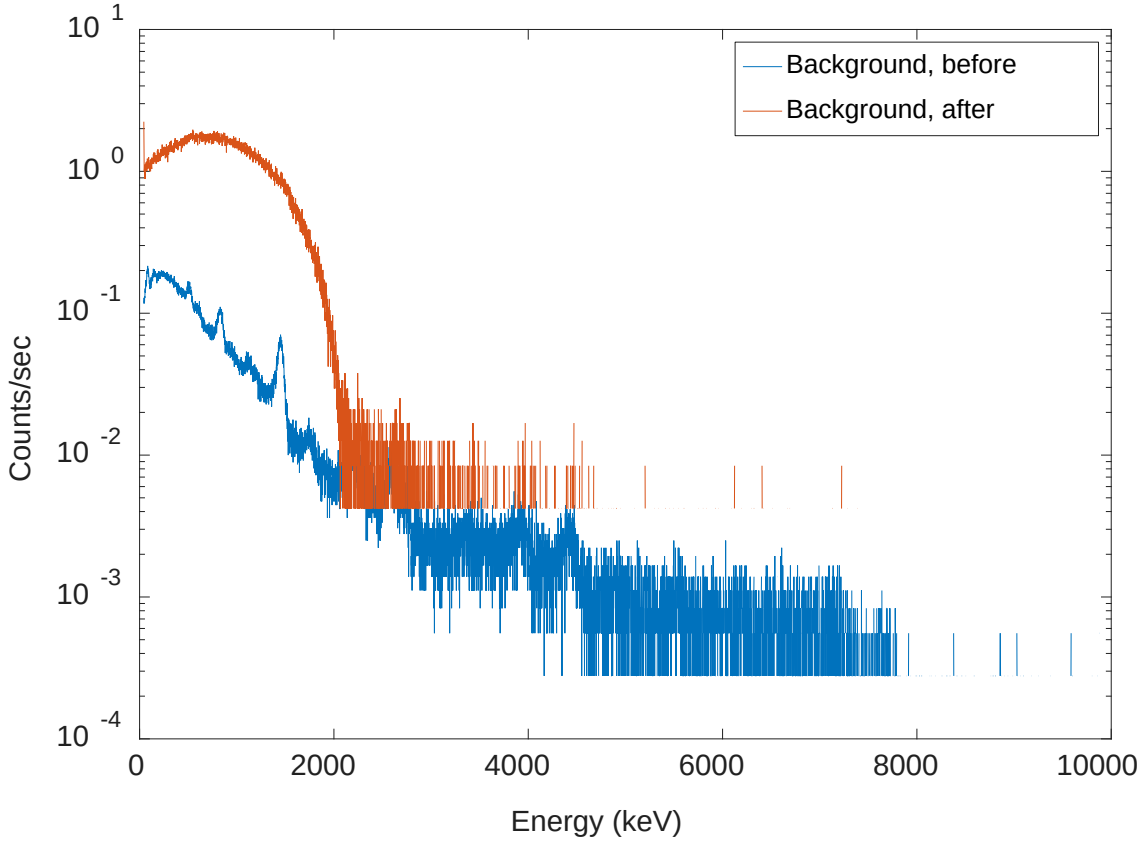


**Figure 30.** Comparison of the background spectra before and after neutron irradiation.

Using the empirical data above as a foundation, analytical estimates for the contributions from $^{128}$I during a typical cylinder assay were developed These calculations assumed that a 5 wt% Type 30B $UF_6$ cylinder emits approximately $4\times10^5$ neutrons/s (total emission rate within the cylinder).

In the presence of the neutron source, the activity of $^{128}$I is given as:

$$\frac{dN_{^{128}I}}{dt} = P_{^{128}I} - \lambda_{^{128}I} N_{^{128}I} \tag{0.3}$$

The following set of integration steps shows the derivation for $N_{^{128}I}(t)$:

$$\frac{dN}{dt} + \lambda N = P$$

$$\frac{dN}{dt} e^{\lambda t} + \lambda N e^{\lambda t} = P e^{\lambda t}$$

$$\frac{d}{dt}\left(Ne^{\lambda t}\right) = Pe^{\lambda t}$$

$$\int \frac{d}{dt}\left(Ne^{\lambda t}\right) = \int_0^t Pe^{\lambda t}$$

$$Ne^{\lambda t} = P\left(\frac{e^{\lambda t}}{\lambda}\Big|_0^t\right)$$

$$\therefore N_{^{128}I}(t) = \frac{P_{^{128}I}}{\lambda_{^{128}I}}\left(1 - e^{-\lambda_{^{128}I}t}\right)$$

Substituting $\phi\Sigma_a$ for $P_{^{128}I}$ we get:

$$N(t)_{^{128}I} = \frac{\phi\Sigma_a}{\lambda_{^{128}I}}\left(1 - e^{-\lambda_{^{128}I}t}\right) \tag{0.4}$$

Using the above, the activity of $^{128}$I can be formulated as:

$$A(t)_{^{128}I} = \lambda_{^{128}I} N(t)_{^{128}I} \tag{0.5}$$

Substituting 1.4 into 1.5, we get:

$$A(t)_{^{128}I} = \phi\Sigma_a\left(1 - e^{-\lambda_{^{128}I}t}\right) \tag{0.6}$$

Equation 1.6 also represents the activity of $^{128}$I immediately upon removing the neutron source after the activation time, $t_a$. Now, the saturation activity, $A_s$, is proportional to $\phi$ and the activation time $t_a$. Likewise, $\phi$ is proportional to neutron emission rate, $S$ (and the distance d away from the source). Keeping the $t_a$ constant (we will relax this assumption later on), count rate $R$, due to the decay of $^{128}$I is only proportional to the neutron emission rate, $S$ thus,

$$R \propto S \tag{0.7}$$

As mentioned earlier, the net count rate of 1673 cps is a result of activation using $^{252}$Cf point source emitting $1.5\times10^7$ neutrons per second (i.e. S) at a distance of 35-cm. By empirically comparing the ratio of the *net count rate to source activity* and by knowing the neutron emission rate of a typical 5% enriched Type 30B cylinder and the exposure times, we can estimate the expected count rate above the background, for a UCVS scenario, as follows:

$$\frac{CR_1}{A_1 \cdot t_1} = \frac{CR_2}{A_2 \cdot t_2} \tag{0.8}$$

Where, $CR_1$ is the net count rate from the $^{252}Cf$ source after irradiation

$A_1$ is the $^{252}Cf$ source activity

$t_1$ is the exposure time in lab

$CR_2$ is the net count rate after irradiation by a 30B cylinder (approximated by scaling the measured $CR_1$ by the neutron emission rate of a 30B cylinder),

$A_2$ is the neutron emission rate of the cylinder, and

$t_2$ is the exposure time when measuring a cylinder (300 seconds)

Substituting the values of these quantities in 1.8 and solving for $CR_2$, we get,

$$\frac{1673}{1.5\times10^{7}\cdot 2081}=\frac{CR_2}{4.04\times10^{5}\cdot 300} \tag{0.9}$$

And therefore, $CR_2$ = 6.5 cps. This is an estimated count rate for the bremsstrahlung spectrum produced by $^{128}I$ immediately following a 5-minute irradiation of the NaI spectrometer by a Type 30B cylinder at enrichment of 5 wt%. This is an approximation scaled from a bare $^{252}Cf$ source located 35-cm away from the detector (approximate distance between center of cylinder and HEVA face) and does not account for the neutron spectra differences, moderation environments, and geometry differences between the small $^{252}Cf$ source and extended-source 30B cylinder.

Building on the analytical estimates above, a higher degree of reality was introduced using MCNP simulations for $^{128}I$ contributions, assuming a UCVS-like measurement geometry that include the HEVA modules positioned near a full cylinder. The simulation process consisted of first determining the production rate of $^{128}I$ via neutron activation in the detector medium from the $^{234}U$ (α,n) neutron spectrum (the dominant source term for enriched cylinders). After quantifying the production yield, a separate MCNP model was created where a uniformly distributed $^{128}I$ beta source was placed in the active detector volume and the photon production (mostly bremsstrahlung) in the detector medium was tallied. Figure 31 below shows the bremsstrahlung photon spectrum obtained from the MCNP simulations.

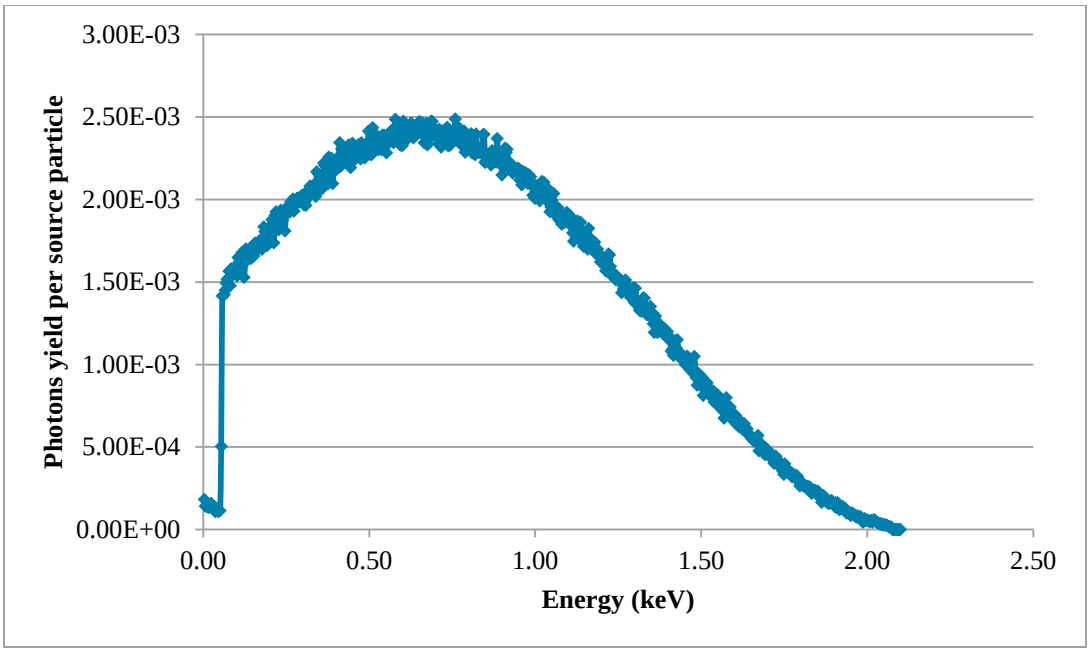


**Figure 31.** Bremsstrahlung photon spectra from $^{128}$I decay in NaI.

Based on these MCNP simulations of a realistic UCVS assay scenario, the calculated production rate of $^{128}$I via the neutron activation is $2.54\times10^{-4}$ per source neutron. Multiplying this result by the gross neutron emission rate ($4.04\text{x}10^{5}$ n/s for 5 wt%) gives an $^{128}$I (in NaI) production rate of 102.6 atoms per second. Considering the fact that a Type 30B cylinder will be measured for five minutes, the induced activity at the end of the measurement is calculated ($102.6*(1-e^{-\lambda t})$, where $\lambda=3.33\text{x}10^{-7}$ $s^{-1}$ and t = 300 s) to be 13.3 Bq. The expected photon count rate due to the induced activity after a five minute cylinder measurement is given as:

$$Count\text{-}rate = \frac{photons}{source\text{-}electron} \times \frac{\#beta}{decay} \times \frac{decay}{s}$$

On average, 0.78 beta particles are emitted for every $^{128}$I decay (NUDAT2). By substituting the photon production yield from MCNP and the above mentioned induced activity, the estimated count rate generated by the $^{128}$I bremsstrahlung spectrum, following a 5-minute cylinder assay, is estimated to be 10.4 cps.

Consistent with intuition, the predicted activation contribution in the simplistic bare-source approximation (6.5 cps) is somewhat lower (~40%) when compared to the UCVS scenario (10.4 cps). Reasons for this include the fact that there is neutron-emitting $UF_6$ close to the detector in the UCVS scenario, room return from the cylinder and surroundings gives a “boost” to the incident neutron flux, and additional moderation from the cylinder and surroundings helps to soften the energy spectrum of the neutron flux incident on the NaI detector. Further, the neutron energy spectrum of the $^{252}$Cf source assumed in the laboratory and analytical estimates differs from that of the $UF_6$ in the cylinder.

The calculations above assume a 5-minute assay period but in facility operations, it may be possible that a cylinder is left in place on the UCVS for long periods of time. The activation produced during that

time may impact the assay of that cylinder or a subsequent cylinder, depending on how quickly that next cylinder is placed on the UCVS. To assess this worst-case scenario, it was assumed that the cylinder is in place for about two hours, during which time the $^{128}$I production rate approaches the saturation activity, creating about 98 Bq of $^{128}$I in the NaI. This translates to a total count rate produced by $^{128}$I of 77.2 cps, approximately 7 times higher than the 5-minute value.

The combination of laboratory, analytical and MCNP analysis described above provides a clear picture of the potential impact of $^{128}$I activation on HEVA. As discussed previously, anticipated count rates for HEVA modules, over the energy range of 50 to 2000 keV impacted by the $^{128}$I bremsstrahlung spectrum, are between 5 and 30 kcps depending on the level of wall deposits in the detector's field of view. By comparison, the short-assay activation contribution to this energy range is ~10 cps, the long-assay contribution approaches 80 cps. It is expected, therefore, that the impact of iodine activation on total HEVA count rate will be negligible (i.e., <0.2% for short assay) for the typical, 5-minute assay. But it remains to be seen whether relative increases are more prominent for specific peaks, for example the 1001-keV since the maximum of the bremsstrahlung spectrum from $^{128}$I peaks is near that energy. For scenarios where cylinders remain on the UCVS for long periods, perturbing effects may become significant; perhaps even on the few-percent level for certain peaks. More investigation is needed, using data from the field trial.

# 7.0 Conclusions

MCNP modeling and analysis has demonstrated that the revised HEVA module design does indeed boost the nontraditional signal efficiency, and via an adaptable design for detector recess, allow tailoring of the field of view to manage the count rate incident on the detector. It is estimated that HEVA count rates could extend as high as ~80 kcps for a worst-case heels scenario, but it is expected that maximum count rates encountered in the field, even for very dirty cylinders, will be less than 30 kcps. For the purpose of the characterization study described in this report, high count rates were considered those up to approximately 100 kcps.

A study of the Osprey parameter space, in the context of the count rates expected for HEVA in the UCVS scenario, has been completed. The following table lists the recommended settings for each of the parameters assessed in this report.

**Table 15.** List of recommended settings for the Canberra Osprey with a NaI(Tl) scintillator, for the HEVA cylinder assay application.

| Parameter | Value/Setting |
|---|---|
| High Voltage | User defined and/or follow manufacturer's recommendation |
| PHA Acquisition times | 60 seconds |
| Gain (Coarse × Fine) | 1×1 |
| Rise-time | 1 µs |
| Flat-top | 0.5 µs |
| BLR Mode | HARD |
| LTC | ON |
| PUR Guard | 2.5x |
| FDisc Mode | Auto |
| FDisc Shaping | Normal |
| Preset | Real-time |
| Dynamic MCA Range | 8192 channels |
| LLD | 0.5 |
| ULD | 100 |

Results presented here indicate that these settings will strike an appropriate balance between count rate throughput and energy resolution. In addition, these settings should ensure that systematic uncertainties introduced by Osprey pulse-processing parameters will be insignificant in the overall HEVA uncertainty budget, so long as input count rates are maintained less than approximately 50 kcps. These findings have informed the hardware and software configurations utilized in the UCVS prototype and long-term field trial.

An investigation of energy calibration approaches indicate that a linear function is most appropriate for determination of the lower bound of the nontraditional region of interest (3.0 MeV), when using a 3-point calibration based on the 186, 765 and 1001-keV lines expected to be available in each cylinder occupancy spectrum.

Laboratory measurement of the intrinsic neutron efficiency for the HEVA nontraditional method produced a value of approximately 0.5 % assuming a region of interest from 3.0 to 8.5 MeV. It was shown that the contribution of the steel layers is relatively small compared to the prompt gamma rays produced in the detector crystal. If HEVA analysis were to use an ROI of 6 -8.5 MeV, the contributions from the steel layers become much more significant, but the total count rate is substantially lower than for the broader energy window.

The potential impact of activation of the NaI(Tl) detector medium was investigated, where the dominant contributor was shown to be the production of $^{128}$I via the activation of $^{127}$I. A combination of laboratory, analytical and MCNP analysis showed that the $^{128}$I bremsstrahlung spectrum will contribute approximately 10 cps in the energy region between 50 and 2000 keV, at the end of a 5-minute cylinder assay. For a 2-hour assay, the count rate may be nearly 8 times higher. It is expected, given nominal total HEVA count rates of 5 to 30 kcps during cylinder assay, that the impact of iodine activation on total HEVA count rate will not be significant. But it remains to be seen whether the impact is significant for key peaks that may be used in enrichment assay methods, for example the 1000-keV region, where the bremsstrahlung spectrum from $^{128}$I peaks.

# 8.0 References


[1] J. N. Cooley, "Model Safeguards Approach and Innovative Techniques Implemented by the IAEA at Gas Centrifuge Enrichment Plants," in *48th Annual Meeting of the Institute of Nuclear Materials Management (INMM)*, Tucson, AZ, 2007.

[2] A. Lebrun, S. C. Kane, L. Bourva, S. Poirier, N. E. Loghin, and D. Langlands, "Improved verification methods for safeguards verifications at enrichment plants," in *Advancements in Nuclear Instrumentation Measurement Methods and their Applications (ANIMMA), 2009 First International Conference on*, 2009, pp. 1-8.

[3] L. E. Smith, A. R. Lebrun, and R. Labella, "Potential Roles of Unattended Safeguards Instrumentation at Centrifuge Enrichment Plants," *Journal of Nuclear Materials Management*, 2013.

[4] "Unattended Cylinder Verification Station, SP-1 Task Proposal," IAEA Department of Safeguards2013.

[5] L. E. Smith, "User Requirements, Unattended Cylinder Verification Station," IAEA Department of Safeguards SG-UR-12186, 2013.

[6] L. E. Smith, D. V. Jordan, A. C. Misner, E. K. Mace, and C. R. Orton, "Hybrid Enrichment Assay Methods for a UF6 Cylinder Verification Station (PNNL-SA-73766)," presented at the 51st Annual Meeting of the Institute of Nuclear Materials Management, Baltimore, MD, 2010.

[7] L. E. Smith, E. K. Mace, A. C. Misner, and M. W. Shaver, "Signatures and Methods for the Automated Nondestructive Assay of Cylinders at Uranium Enrichment Plants (PNNL-SA-69410)," *IEEE Transactions on Nuclear Science*, vol. 57, pp. 2247-2253, 2010.

[8] B. S. McDonald, D. V. Jordan, C. T. Orton, E. K. Mace, R. S. Wittman, and L. E. Smith, "Model and Algorithm Evaluation for the Hybrid UF6 Container Inspection System (PNNL-SA-77483)," presented at the 52nd INMM Annual Meeting, Palm Desert, CA, 2011.

[9] L. E. Smith, K. A. Miller, E. K. Mace, D. V. Jordan, C. R. Orton, C. D. Rael, *et al.*, "A Study of Candidate NDA Methods for Unattended UF6 Cylinder Verification: Action Sheet 40 Final Report," PNNL-22954, 2014.

[10] L. E. Smith, D. V. Jordan, J. A. Kulisek, B. S. McDonald, and E. K. Mace, "Viability of UF6 Cylinder Verification using the Hybrid Enrichment Verification Array (PNNL-SA-102233)," *Journal of Nuclear Materials Management (submitted)*, 2015.

[11] "The UF6 manual, Good Handling Practices for Uranium Hexafluoride," USEC, USEC Inc., 6903 Rockledge Drive, Bethesda, MD 20817July 2006 2006.

[12] D. V. Jordan, L. E. Smith, J. A. Kulisek, B. S. McDonald, and E. K. Mace, "Hybrid Enrichment Assay Methods for a UF6 Cylinder Verification Station: FY13 Final Report," Pacific Northwest National Laboratory (PNNL), Richland, WA (US) PNNL-23164, 2013.

[13] T. Goorley, M. James, T. Booth, F. Brown, J. Bull, L. Cox, *et al.*, "Initial MCNP6 release overview," *Nuclear Technology*, vol. 180, pp. 298-315, 2012.

[14] J. Wilks, "Uranium Conversion and Enrichment," in *Nuclear fuel cycles and engineering*, I. Crossland, Ed., ed: Woodhead Publishing, 2012.

[15] M. Sheaffer, S. Keeton, and H. Lutz, "Nuclear Criticality Safety Evaluation of Large Cylinder Cleaning Operations Inx-705, Portsmouth Gaseous Diffusion Plant," UCRL-ID--121163, 1995.

[16] C. W. Shockley, "Radiation Levels on Empty Cylinders Containing Heel Materials," presented at the Second International Conference Uranium Hexafluoride Handling, Oak Ridge, Tennessee, 1991.

[17] T. Watanabe, T. Nakabayashi, and Y. Kamei, "Cleaning and Inspection Experience of $UF_6$ 30B Cylinders," presented at the Conference on Uranium Hexafluoride---Safe Handling, Processing, and Transporting, Oak Ridge, Tennessee, 1988.

[18] L. E. Smith, K. D. Jarman, R. S. Wittman, M. A. Zalavadia, and J. March-Leuba, "Modeling and Analysis Methods for an On-Line Enrichment Monitor ( PNNL-SA-112223)," *Journal of Nuclear Materials Management (submitted)*, 2015.

[19] *Basic Counting Systems, Canberra Industries, Inc*.
Available: http://www.canberra.com/fr/literature/fundamental-principles/pdf/Basic-Counting-System.pdf

[20] G. F. Knoll, *Radiation detection and measurement*: John Wiley & Sons, 2010.

[21] "Osprey Universal Digital MCA Tube Base - User's Manual," ed: Canberra Industries, Inc.

[22] G. Gilmore, *Practical gamma-ray spectroscopy*: John Wiley & Sons, 2011.

[23] J. A. Kulisek, D. V. Jordan, E. K. Mace, B. S. McDonald, and L. E. Smith, "Hybrid Enrichment Verification Array: Investigations of the High-Energy Gamma-Ray Signature Origin and Use for Partial Defect Detection (PNNL-SA-104092)," in *INMM Annual Meeting Proceedings*, 2014.

[24] M. Ellis, L. Mitchell, S. Jackson, J. Zier, J. O'Malley, J. Threadgold, *et al.*, "Activation of sodium iodide detectors in an Active Interrogation environment," in *IEEE Nuclear Science Symposium and Medical Imaging Conference*, 2012, pp. 11-17.

Pacific Northwest
NATIONAL LABORATORY

*Proudly Operated by* **Battelle** *Since 1965*

U.S. DEPARTMENT OF
ENERGY

902 Battelle Boulevard
P.O. Box 999
Richland, WA 99352
**1-888-375-PNNL** (7665)

***www.pnnl.gov***